Atmos. Chem. Phys. Discuss., https://doi.org/10.5194/acp-2017-754
Manuscript under review for journal Atmos. Chem. Phys.
Discussion started: 13 October 2017
© Author(s) 2017. CC BY 4.0 License.

Atmospheric Chemistry and Physics Discussions

Investigating the role of dust in ice nucleation within clouds and further effects on regional weather system over East Asia

Part I: model development and validation

Lin Su[1], and Jimmy C.H. Fung[2, 3]

[1] School of Science, Hong Kong University of Science and Technology, Hong Kong, China

[2] Division of Environment, Hong Kong University of Science and Technology, Hong Kong, China

[3] Department of Mathematics, Hong Kong University of Science and Technology, Hong Kong, China

Correspondence to: Lin Su (lsu@connect.ust.hk)

Keywords: dust; ice nucleation; microphysics scheme implementation; numerical modeling

Highlights:

An aerosol model has been coupled with a microphysics scheme for evaluating the role of dust particles in atmospheric ice nucleation.

The effect of dust on atmospheric ice water content over East Asia during a dust-intensive period is simulated.

The simulation of atmospheric ice water content during dust events is substantially improved upon the effect of dust being considered.

Atmos. Chem. Phys. Discuss., https://doi.org/10.5194/acp-2017-754
Manuscript under review for journal Atmos. Chem. Phys.
Discussion started: 13 October 2017
© Author(s) 2017. CC BY 4.0 License.

Abstract. The GOCART–Thompson microphysics scheme, which couples the Goddard Chemistry Aerosol Radiation and Transport (GOCART) model and aerosol-aware Thompson microphysics scheme, has been implemented in the Weather Research and Forecast model coupled with Chemistry (WRF-Chem), to quantify and evaluate the effect of dust on the ice nucleation process in the atmosphere by serving as ice nuclei. The performance of the GOCART-Thompson microphysics scheme in simulating the effect of dust in atmospheric ice nucleation is then evaluated over East Asia during spring in 2012, a typical dust-intensive season. Based upon the dust emission reasonably reproduced by WRF-Chem, the effect of dust on atmospheric cloud ice water content is well reproduced. With abundant dust particles serving as ice nuclei, the simulated ice water mixing ratio and ice crystal number concentration increases by one order of magnitude over the dust source region and downwind areas during the investigated period. The comparison with ice water path from satellite observations demonstrated that the simulation of cloud ice profile is substantially improved by applying the GOCART–Thompson microphysics scheme in the simulations. Additional sensitivity experiments are carried out to optimize the parameters in the ice nucleation parameterization in the GOCART–Thompson microphysics scheme, and the results suggest that the calibration factor in the ice nucleation scheme should be set to 3 or 4. Lowering the threshold relative humidity with respect to ice to 100% for the ice nucleation parameterization leads to further improvement in cloud ice simulation.

Atmos. Chem. Phys. Discuss., https://doi.org/10.5194/acp-2017-754
Manuscript under review for journal Atmos. Chem. Phys.
Discussion started: 13 October 2017
© Author(s) 2017. CC BY 4.0 License.

Atmospheric Chemistry and Physics Discussions

1 Introduction

As one of the largest natural aerosol sources, dust aerosol contributes considerably to the global aerosol burden (Textor et al., 2006). The Intergovernmental Panel on Climate Change (IPCC) has recognized dust as a major component of atmospheric aerosols, which are an "essential climate variable." East Asia is a major contributor to the Earth's dust emission. It has been reported in previous studies that East Asian dust contributes 25–50% of global emission, depending on the climate of the particular year (Ginoux et al., 2001).

Dust in the atmospheric can alter the Earth's radiation budget through certain ways. By reflecting, absorbing and scattering the incoming solar radiation, dust can cause a warming effect within the atmosphere, and a cooling effect at the surface layer (Lacis, 1995). Dust within clouds can absorb short-wave and long-wave radiation and heat up the surrounding environment, causing a shrinking of cloud, and a lower cloud albedo (Perlwitz and Miller, 2010;Hansen et al., 1997). Moreover, dust particles are recognized as effective ice nuclei, and play an important role in the ice nucleation process in the atmosphere, directly affecting the dynamics in ice and mixed-phase clouds, such as the formation and development of clouds and precipitation (Koehler et al., 2010;Twohy et al., 2009).

To date, Many studies have been conducted to evaluate the direct radiative effect of dust aerosol using radiation schemes implemented in numerical models all over the world (Mallet et al., 2009;Nabat et al., 2015a;Ge et al., 2010;Hartmann et al., 2013;Huang et al., 2009;Bi et al., 2013;Liu et al., 2011a;Liu et al., 2011b;Huang, 2017). Recently, semi-direct effect of dust has been investigated in a few studies over different regions by applying various global and regional models (Tesfaye et al., 2015;Nabat et al., 2015b;Seigel et al., 2013). Unfortunately, due to the poor understanding on the dust-cloud-interaction in microphysics processes, quantifying the microphysical effect of dust remains as a difficult problem. Various ice nucleation parameterizations have been implemented into global models to estimate the importance of dust in atmospheric ice nucleation (Lohmann and Diehl, 2006;Karydis et al., 2011;Hoose et al., 2008;Zhang et al., 2014). However, most regional models are not capable of estimating the indirect effect of dust, and vary rare work has been done to assess the indirect effects of dust on the weather system, especially over East Asia, which is a major contributor to the global dust emission. Currently, only a few microphysics schemes considering aerosol-cloud-interaction are implemented in regional, and in most of these microphysics schemes, only the cloud condensation nuclei served by aerosols are considered (Perlwitz and Miller, 2010;Solomos et al., 2011;Miller et al., 2004), with the ice nuclei not treated, or represented by a prescribed ice nuclei distribution (Chapman et al.,

© Author(s) 2017. CC BY 4.0 License.

2009;Baró et al., 2015), and the number of predicted ice crystals is a function of temperature or ice saturation. In reality, however, the number of ice crystals that can form in the atmosphere is highly dependent on the number of particles that can act as ice nuclei, and dust is the most abundant aerosols that can effectively serve as ice nuclei and affect the formation and development of mixed-phase and ice clouds in the atmosphere. This effect should not be neglected in numerical models, especially in the simulations over arid regions during strong wind events (DeMott et al., 2003;Koehler et al., 2010;DeMott et al., 2015;Lohmann and Diehl, 2006;Atkinson et al., 2013).

The GOCART aerosol model, which has been implemented in WRF-Chem, is one of the most widely-used aerosol models for global and regional dust simulation (Chen et al., 2014;Ashrafi et al., 2017;Chiao et al., 2016;Rizza et al., 2017;Flaounas et al., 2017;Kumar et al., 2014). It is coupled with various radiation schemes for evaluating the radiative effects induced by dust in WRF-Chem. However, it is not linked with any microphysics scheme, therefore, the indirect effect of dust cannot be calculated in the model.

Since 2014, the aerosol-aware Thompson microphysics scheme, which takes into account the aerosols serving as ice nuclei, has been implemented into WRF, enabling the model to explicitly predict the droplet number concentration for cloud droplets through the number concentrations of cloud condensation nuclei and ice nuclei (Thompson and Eidhammer, 2014). Therefore, the aerosol-aware Thompson scheme is an ideal microphysics scheme for evaluating the effect of dust in atmospheric ice nucleation processes. However, this scheme is not coupled with any aerosol model in WRF-Chem. When the aerosol-aware Thompson microphysics scheme is activated, the model reads in pre-given monthly-averaged climatological aerosol data derived from the output of other global climate model, which introduces large errors into the estimation of the effects of dust in microphysical processes, especially in real-time simulations.

In light of the above, we aimed to fully couple the aerosol-aware Thompson microphysics scheme with an aerosol model in the WRF-Chem modeling system in this study, enabling the model to simulate the effect of dust aerosol in ice nucleation processes during online simulations, for investigating the role that East Asian dust plays in the ice nucleation process in the atmosphere.

The remainder of the manuscript is presented as follows. Section 2 provides a description of the model including the implementation work for coupling the aerosol-aware Thompson microphysics scheme and the GOCART aerosol model in WRF-Chem, followed by the model configurations for numerical simulations in section 3. Section 4 presents

© Author(s) 2017. CC BY 4.0 License.

89 the observational data used to validate the performance of the newly–implemented GOCART-Thompson
90 microphysics scheme. Section 5 is the results and discussion, followed by the conclusions section 6.

91

92 **2 Model description**

93 WRF-Chem is an online-coupled regional modeling system, which means that it can simultaneously simulate the
94 meteorological field, the chemical field, and the interaction in between (Grell et al., 2013). The chemical model
95 contains several gas- and aerosol-phase chemical schemes. In this study, we focus on the GOCART model, a simple
96 aerosol model that will be used for dust simulation.

97

98 **2.1 GOCART aerosol model**

99 GOCART is an aerosol model for simulating major tropospheric aerosol components, such as sulfate, dust, black
100 carbon, organic carbon, and sea-salt aerosols (Ginoux et al., 2001;Chin et al., 2000). It has been implemented into
101 WRF-Chem as a bulk aerosol scheme. GOCART is a simple aerosol scheme that can predict the mass of aerosol
102 components, but does not account for complex chemical reactions. Therefore, it is numerically efficient in simulating
103 aerosol transport, and thus applicable to cases without many chemical processes, especially dust events.

104 Shao's dust emission scheme is one of the three dust emission schemes in the GOCART aerosol model (Kang et al.,
105 2011;Shao, 2004, 2001;Shao et al., 2011), and has been demonstrated to exhibit superior performance in reproducing
106 the dust cycle over East Asia compared to other emission schemes (Su and Fung, 2015). The Shao's emission scheme
107 was updated in WRF-Chem since version 3.8 released in 2016, to produce five size bins for dust emission, with
108 diameters of < 2 μm, 2–3.6 μm, 3.6–6.0 μm, 6.0–12.0 μm, and 12.0–20.0 μm, and mean effective radii of 0.73 μm,
109 1.4 μm, 2.4 μm, 4.5 μm, and 8.0 μm.

110

111 **2.2 Aerosol-aware Thompson microphysics scheme**

112 The Thompson scheme is a bulk two-moment microphysics scheme that considers the mixing ratios and number
113 concentrations for five water species: cloud water, cloud ice, rain, snow and a hybrid graupel/hail category. The

© Author(s) 2017. CC BY 4.0 License.

aerosol-aware version of the Thompson scheme incorporates the activation of aerosols serving as cloud condensation nuclei and ice nuclei, and therefore it explicitly predicts the droplet number concentration of cloud water as well as the number concentrations of cloud condensation nuclei and ice nuclei. Hygroscopic aerosols that serve as cloud condensation nuclei are referred to as water-friendly aerosols, and those non-hygroscopic ice-nucleating aerosols are referred to as ice-friendly aerosols. The cloud droplets nucleate from explicit aerosol number concentration using a look-up table for the activated fraction as determined by the predicted temperature, vertical velocity, number of available aerosols, and pre-determined values of the hygroscopicity parameter and aerosol mean radius, while the nucleation of ice crystals by dust particles follows the parameterization of DeMott et al. (DeMott et al., 2010) to account for condensation and immersion freezing, and the parameterization of Phillips et al. (Phillips et al., 2008) to account for deposition nucleation. Freezing of super-cooled water droplet is determined following the Bigg's parameterization (Bigg, 1953), but with a temperature adjustment of a few degrees depending on dust concentration (Thompson and Eidhammer, 2014). In the current version of WRF-Chem, the number concentrations of both water-friendly aerosols and ice-friendly aerosols are pre-given in the initialization of the simulations, and are derived from the climatological data produced by global model simulations in which particles and their precursors are emitted by natural and anthropogenic sources and explicitly modeled with multiple size bins for multiple species of aerosols by the GOCART model. In the consequent simulations, a fake aerosol emission is implemented by giving a variable lower boundary condition based on the initial near-surface aerosol concentration and a simple mean surface wind for calculating a constant aerosol flux at the lowest level in the model. The number concentrations of both water-friendly aerosols and ice-friendly aerosols are then updated at every time step by summing up the fake aerosol emission fluxes and tendencies induced by aerosol-cloud-interaction. The limitation of the current aerosol-aware Thompson scheme is that the aerosol profile generated from a fake emission can hardly represent the realistic aerosol level, leading to great errors in quantifying the indirect effects of aerosols.

2.3 Implementation of GOCART-Thompson microphysics scheme

To investigate the real-time indirect effects of dust aerosol over East Asia, modifications have been made to couple the GOCART model with the aerosol-aware Thompson microphysics scheme. The modifications were based on WRF-

© Author(s) 2017. CC BY 4.0 License.

Chem version 3.8.1, and consisted of three parts, modification of the GOCART aerosol scheme, modification of the aerosol-aware Thompson microphysics scheme, and the introduction of a new wet removal scheme.

2.3.1 Upgraded GOCART aerosol model

Currently, the GOCART aerosol model generates only the mass concentration for aerosols but no number concentrations. However, the number concentration of aerosols are required for a microphysics scheme to evaluating the indirect effects of aerosols. Therefore, modification was needed to provide information about the number concentrations of aerosols from the mass concentration produced in GOCART aerosol model.

The aerosol mass concentration was converted into number concentration using the aerosol density and effective radius for each size bin. Assuming that dust particles are spherical, the mass per dust particle (m_p, μg/#) for a size bin can be approximated through the mean effective radius and density for that size bin.

$$m_p = \rho_{dust} \times \frac{4}{3} \times \pi r_{dust}^3 \quad (1)$$

where ρ_{dust} and r_{dust} are the dust density and mean effective radius, respectively, for a particular size bin.

The aerosol number concentration *N (#/kg)* for size bin *n* at a grid point *(i, j, k)* is then calculated by the following equation:

$$N(i, j, k, n) = C(i, j, k, n) / m_p \quad (2)$$

where *C(i, j, k, n)* is the dust mass mixing ratio *(μg/kg)* for size bin n at grid point *(i, j, k)*. Summing up the aerosol number concentrations through all of the size bins gives a total dust number concentration, which will be passed into the Thompson microphysics scheme. Note that all of the dust particles are treated as ice-friendly aerosols in this study, and represented by a newly-introduction variable, ice–friendly aerosol produced by GOCART aerosol model (*GNIFA)*.

$$GNIFA(i, j, k) = \sum_{i=1}^{n} N(i, j, k, n) \quad (3)$$

2.3.2 Ice nucleation parameterization

Atmos. Chem. Phys. Discuss., https://doi.org/10.5194/acp-2017-754
Manuscript under review for journal Atmos. Chem. Phys.
Discussion started: 13 October 2017
© Author(s) 2017. CC BY 4.0 License.

Atmospheric Chemistry and Physics Discussions

In the aerosol-aware Thompson scheme, the condensation and immersion freezing above water saturation in the ice nucleation process is determined following the DeMott's parameterization proposed in 2010 (hereafter DeMott2010 scheme) based on combined data from field experiments at a variety of locations over 14 years (DeMott et al., 2010), to account for condensation and immersion freezing. In the DeMott2010 scheme, the relationship between ice nuclei number concentration and ice crystal number concentration is as follows:

$$n_{ice,T_k} = a(273.16 - T_k)^b n_{aero}{}^{(c(273.16-T_k)+d)} \quad (4)$$

where n_{ice,T_k} is the ice crystal number concentration (std L^{-1}) at temperature of T_k; n_{aero} is the number concentration of ice-friendly aerosols (std cm^{-3}), and a, b, c, and d are constant coefficients equal to 5.94×10^{-5}, 3.33, 2.64×10^{-2}, and 3.33×10^{-3}, respectively. The parameterization was tested with various temperatures and number concentration of ice-friendly aerosols, yielding a good performance in reproducing ice crystal number concentration under conditions of relatively low mixing ratio of water vapor or low concentration of ice crystals compared with field–experimental data. The relationship between simulated ice nuclei number concentration and ice crystal number concentration is basically linear for concentrations of both of under 1,000 std cm^{-3} (DeMott et al., 2010).

The above parameterization was further developed in 2015 (hereafter the DeMott2015 scheme) for conditions of higher mixing ratio of water vapor or higher concentrations of ice crystals based on the latest data from field and laboratory experiments. According to the latest observational data, ice crystal number concentration increases exponentially with ice-friendly aerosol number concentration, and existing aerosols with relatively low concentrations (less than 1,000 std cm^{-3}) can produce a large number of ice crystals (more than 100,000 std L^{-1}). The updated relationship between ice nuclei number concentration and ice crystal number concentration in the Demott2015 parameterization scheme is as follows.

$$n_{ice,T_k} = c_f n_{aero}^{\alpha(273.16-T_k)+\beta} \exp(\gamma(273.16 - T_k) + \delta) \quad (5)$$

where α, β, γ, and δ are constant coefficients equal to 0, 1.25, 0.46, and -11.6, respectively. The calibration factor c_f ranges from 1 to 6, and is recommended to be 3. The updated parameterization shows a good performance in reproducing ice crystal with relatively high concentration in ice nucleation involving ice-friendly aerosols under varying temperature and aerosol number concentration.

© Author(s) 2017. CC BY 4.0 License.

188 The number concentrations of ice crystals that produced by the DeMott2015 scheme is much higher than that produced
189 by the DeMott2010 scheme when applied to the same value of n_{aero}, and the difference grows larger with decreasing
190 temperature and increasing number concentration of ice-friendly aerosols (DeMott et al., 2015). As the DeMott2015
191 scheme has been examined using more comprehensive field– and laboratory–experimental data, we apply the
192 DeMott2015 ice nucleation scheme in the GOCART–Thompson microphysics scheme, instead of the DeMott2010
193 scheme in the default aerosol-aware Thompson microphysics scheme to simulate the ice nucleation involving dust.

194 Originally, the calibration factor c_f is set to be 3; the threshold temperature is set to be –20 °C. The ice nucleation
195 process is triggered once the relative humidity with respect to ice (RH_i) exceeds 105%. Furthermore, when the relative
196 humidity with respect to water (RH_w) is above 98.5%, it is counted as condensation and immersion freezing, and
197 calculated by DeMott2015 scheme; when RH_w is below 98.5%, it is treated as deposition nucleation, and determined
198 by the Phillips parameterization (Phillips et al., 2008).

199

200 **2.3.3 GOCART-Thompson microphysics scheme**

201 Firstly, the initialization module for the aerosols in the aerosol-aware Thompson scheme was modified. The
202 initialization module used to read in pre-given climatological aerosol data at the first time step of the simulation, which
203 provided an annual mean of the global distribution of the number concentrations of the water-friendly and ice-friendly
204 aerosols in the aerosol-aware Thompson microphysics scheme. In the GOCART–Thompson microphysics scheme,
205 the initialization module was removed, instead, the scheme was modified to read in the bulk number concentration of
206 aerosols produced by the GOCART aerosol model updated at every time step.

207 Secondly, the bulk number concentration of ice-friendly aerosols read in from the GOCART aerosol model is passed
208 into the GOCART–Thompson microphysics scheme for the calculation of the number concentration of ice nucleating
209 particles.

210 Based on the modification above, the deposition rate of the ice-friendly aerosols at grid point *(i, j, k)*, which is the
211 tendency of ice-friendly aerosols in terms of number concentration due to the ice nucleation process at this grid point,
212 is calculated.

Atmos. Chem. Phys. Discuss., https://doi.org/10.5194/acp-2017-754
Manuscript under review for journal Atmos. Chem. Phys.
Discussion started: 13 October 2017
© Author(s) 2017. CC BY 4.0 License.

After the microphysical processes are finished for a particular time step, the tendency term (ten_{dust}, *#/kg/s*) for the bulk aerosol number concentration produced by the microphysics scheme is then passed into a wet scavenging scheme to calculate the loss of aerosol mass due to the ice nucleation process, as well as the collision-collection by precipitations within clouds. Finally, the aerosol mass field can be updated.

2.3.4 In-cloud wet scavenging

As no in-cloud scavenging is considered for dust aerosol in WRF-Chem, a new wet scavenging process was then introduced into WRF-Chem to calculate the loss of aerosol mass due to the microphysical processes within clouds using the tendency of aerosol number concentration produced by the microphysics scheme. Assuming that the collection of dust particles is proportional to the number concentration, the fraction of dust particle for each size bin can be calculated in the GOCART aerosol model:

$$\varphi(i, j, k, n)=\frac{N(i,j,k,n)}{GNIFA(i,j,k)} \quad (6)$$

The tendency of ice-friendly aerosol is then distributed into each size bin and the loss of dust mass due to the microphysical processes for a particular size bin *n* is calculated by the following equation:

$$wetscav(i, j, k, n)= ten_{dust}\ (i, j, k)\times \varphi(i, j, k, n)\times m_p \times dt \quad (7)$$

where *dt* is the time step for the simulation.

The mass mixing ratio for dust aerosol in a particular size bin *n* is then updated for the following simulation at the next time step:

$$C(i, j, k, n)= C(i, j, k, n)-wetscav(i, j, k, n) \quad (8)$$

Apart from the in-cloud scavenging, the below-cloud wet removal is calculated by the default wet deposition scheme in the GOCART aerosol model, in which the wet removal of dust is proportional to concentration.

3 Model configurations

© Author(s) 2017. CC BY 4.0 License.

A numerical experiment was conducted to examine the performance of the newly-implemented GOCART–Thompson microphysics scheme in simulating the ice nucleation process induced by dust in the atmosphere. According to the observations, the dust events in 2012 were concentrated in mid-March to late-April, and the satellite observations from mid-March to the end of April were available for model validation; therefore, the simulation period for this numerical test was from March 9 to April 30, 2012, with the first eight days as "spin-up" time. Only the results from March 17 to April 30, 2012 were used for further analysis. The final reanalysis data provided by the United States National Center of Environmental Prediction with a horizontal resolution of one degree was used for generating the initial and boundary conditions for the meteorological fields, and the simulations were re-initialized every four days, with the aerosol field being re-cycled, which means that the output of the aerosol field from the previous four-day run was used as the initial aerosol state for the subsequent four-day run.

Two nested domains were used for the simulation, as shown in Figure 1. The outer domain (domain 1) is in a horizontal resolution of 27 km, and covers the entire East Asia region. The inner domain (domain 2) is in a horizontal resolution of 9 km, and covers the entire central to East China. Both domains have 40 vertical layers, with the top layer at 50 hPa. The locations of the two major dust sources, the Taklimakan Desert and the Gobi Desert, are marked in Figure 1.

Two simulations were conducted for the numerical test. One control run (CTRL) was conducted without dust and one test run (DUST) was conducted with dust, both using the newly–implemented GOCART–Thompson microphysics scheme. The GOCART aerosol model was applied to simulate aerosol processes (Ginoux et al., 2001;Ginoux et al., 2004). Shao's dust emission (Kang et al., 2011;Shao et al., 2011) with soil data from the United states Geological Survey (Soil Survey Staff, 1993), which have been demonstrated to have good performance in reproducing dust emissions over East Asia were used to generate dust emission in the test run. The new wet scavenging scheme was used for in-cloud wet scavenging of aerosols due to microphysical processes. Other important physical and chemical parameterizations applied for the simulations are as follows. The Mellor–Yamada–Janjic (MYJ) turbulent kinetic energy scheme was used for the planetary boundary layer parameterization (Janjić, 2002, 1994); the moisture convective processes were parameterized by the Grell-Freitas scheme (Grell and Freitas, 2014); the short-wave (SW) and long-wave (LW) radiation budgets were calculated by the Rapid Radiative Transfer Model for General Circulation (RRTMG) SW and LW radiation schemes (Mlawer et al., 1997;Iacono et al., 2008), the gravitational settling and

© Author(s) 2017. CC BY 4.0 License.

surface deposition were combined for aerosol dry deposition calculation (Wesely, 1989); a simple washout method was used for the below-cloud wet deposition of aerosols; and the aerosol optical properties were calculated based on the volume-averaging method. As no dust emission is produced in CTRL, the setting for ice nucleation process in CTRL followed the dust-free case in the original aerosol-aware Thompson scheme. The background concentration of ice nuclei was set to be 1/L for the freezing of super-cooled water droplets into cloud ice, which was accounted by the Bigg's parameterization (Bigg, 1953); the initiation of ice nucleation was determined by a temperature-dependent function following Cooper (Cooper, 1986) when the temperature was below –20 °C, and RH_i exceeded 105% (Thompson and Eidhammer, 2014).

4 Observations

4.1 Surface PM_{10} observations

The hourly observations of surface PM_{10} concentration at ten environmental monitoring stations located in or surrounding the dust source areas in East Asia were used to examine the capability of the model in reproducing the trend and magnitude of dust levels at the ground surface during the simulation period. The ten stations were located in Jinchang, Gansu Province, Yinchuan, Qinghai Province, Shizuishan, Ningxia Province, Baotou, Inner Mongolia, and Yan'an, Shaanxi Province. The location of the ten stations are indicated by the blue dots in Figure 1.

4.2 AERONET AOD observations

The AERONET program is a ground-based aerosol remote sensing network for measuring aerosol optical properties at sites distributed around the globe. This program provides a long-term database of aerosol optical properties such as aerosol extinction coefficient, single-scattering albedo, and aerosol optical depth (AOD) measured at various wavelength. The AOD represents the total amount of aerosols within the atmospheric column. The observational data from two sites were available for comparison with the simulation results during the simulation period in this study. One was Dalanzadgad located to the north of the Gobi Desert in Mongolia, and the other was the Semi-Arid Climate and Environment Observatory of Lanzhou University (SACOL) located at Lanzhou, Gansu Province, China. The exact

© Author(s) 2017. CC BY 4.0 License.

locations of the two AERONET sites are depicted by the red triangles in Figure 1. All of the measured data had passed the quality control standard level 2, with an uncertainty of ±0.01 (Holben et al., 2001).

4.3 Satellite data

4.3.1 Multi-angle Imaging SpectroRadiometer (MISR)

The MISR instrument aboard the Terra platform of the United State National Aeronautics and Space Administration (NASA) has been monitoring aerosol properties globally since 2000. It observes the aerosol properties in four narrow spectral centered at 443 nm, 555 nm, 670 nm, and 865 nm, due to which the aerosol properties even over highly bright surfaces, such as deserts, can be retrieved (Martonchik et al., 2004;Diner et al., 1998). In this study, the AOD data at 555 nm retrieved from the MISR level 3 products with a spatial resolution of 0.5° were used for comparison with the spatial distribution of simulated AOD over East Asia during the investigated period.

4.3.1 Moderate Resolution Imaging Spectroradiometer (MODIS)

The MODIS instruments aboard Terra and Aqua platforms of NASA monitor Earth's changes and provide global high-resolution cloud and aerosol optical properties at a near-daily interval (Kaufman et al., 1997).

To retrieve aerosol information over bright surfaces, such as deserts, the Deep Blue algorithm was developed to employ retrievals from the blue channels of the MODIS instruments, at which wavelength the surface reflectance is very low, such that the presence of aerosol can be detected by increasing total reflectance and enhanced spectral contrast (Hsu et al., 2006). By applying this algorithm, the AOD values at wavelengths of 214 nm, 470 nm, 550 nm, and 670 nm over bright surfaces can be retrieved. In this study, the MODIS level 2 AOD data at a 550 nm with a spatial resolution of 10 km were used for comparison with the simulated AOD during the simulation period.

Furthermore, MODIS combines infrared and visible techniques to detect physical and radiative cloud properties, and a near-infrared algorithm was applied to retrieve the precipitable water vapor, including liquid and ice water content, in the atmosphere (Gao and Kaufman, 1998). The thermal column water vapor path was then derived by integrating the moisture profile throughout the atmospheric column. In this study, the ice water path retrieved from the MODIS

© Author(s) 2017. CC BY 4.0 License.

level 3 cloud products with a spatial resolution of one degree was used for comparison with simulated ice water path during the simulation period.

4.3.2 Cloud-Aerosol Lidar and Infrared Pathfinder Satellite Observation (CALIPSO)

The Cloud-Aerosol Lidar and Infrared Pathfinder Satellite, which is aboard the Aqua platform of NASA, combines an active Light Detection and Ranging (LIDAR) instrument with passive infrared and visible imagers to probe the vertical structure and properties of thin clouds and aerosols around the globe (Vaughan et al., 2004). It aims to fill existing gaps in the ability to measure the global distribution of aerosols and cloud properties, and provides three-dimensional perspectives of how clouds and aerosols form, evolve, and affect weather and climate. It observes high-resolution vertical profiles of aerosol and cloud extinction coefficient globally at wavelengths of 532nm and 1064 nm. The atmospheric ice water content (IWC) is derived from the observational cloud extinction coefficients at 532 nm (Winker et al., 2009). In this study, the vertical profiles of CALIPSO IWC with a horizontal resolution of 5 km and vertical resolution of 60 m were applied to verify the performance of the model in simulating the vertical distribution of atmospheric ice water content.

5 Results and model validation

5.1 Dust over East Asia

The time series of daily average dust load over the entire East Asia region (domain 1) during the simulation period is shown in Figure 2a. In total four dust events occurred during the simulation period, lasting from March 18 to 25, March 30 to April 7, April 9 to 19, and April 22 to 29, 2012. The case from April 22 to 29 was the most significant one, with daily s dust mass load of double the other cases. The fraction of daily dust load for each size bin is also shown in Figure 2a. The dust particles in the third, fourth and fifth bins with effective diameters ranging from 3.6 to 20 μm account for the major part of the total mass of dust aerosols, and dust particles with diameters smaller than 3.6 μm account for a minor fraction of the total mass of dust aerosols.

© Author(s) 2017. CC BY 4.0 License.

337 The time series of the daily average number density of dust particles over East Asia during the simulation period
338 shown in Figure 2b shows a similar distribution as that for dust load; the noteworthy distinction between the time
339 series for dust load and number density lies in the fraction of each size bin. The two size bins with the smallest
340 diameters (no larger than 3.6 μm) account for over 80% of the total number of dust particles, and the particles with
341 diameters smaller than 6 μm account for over 95% of the total number of dust particles, indicating that the smallest
342 dust particles are the main source of ice-friendly aerosol to serve as ice nuclei in the atmosphere.

343

344 **5.1.1 Surface PM_{10} concentration**

345 To evaluate the performance of WRF-Chem in reproducing dust emission over East Asia, the simulated surface PM_{10}
346 concentration were compared with observations from ten environmental monitoring stations located near dust sources
347 and downwind areas. The time series of the observed and simulated surface PM_{10} concentrations at the ten stations
348 during the simulation period are shown in Figure 3. Overall, the model shows a good performance in simulating the
349 dust cycle at different stations, with the trend and magnitude of the daily mean PM_{10} concentration well captured at
350 most of the stations, although the surface PM_{10} concentration was overestimated at one station in Jinchang during the
351 simulation period (Figure 3e), and the dust event on April 26 was also overestimated at the stations in Shizuishan
352 (Figure 3c and d) and Yinchuan (Figure 3i and j).

353 The performance statistics for the simulated results are shown in Table 1. The model tends to produce lower surface
354 PM_{10} concentrations than those observed, as no other emissions were considered in the simulations. The mean bias
355 (MB) ranged from −108.73 μg/m^3 to 72.46 μg/m^3, with a mean over all of the stations of −18.84 μg/m^3. The mean
356 error (ME) ranged from 46.07 μg/m3 to 155.83 μg/m3, with a mean over all of the stations of 107.24 μg/m^3. The root
357 mean squared error (RMSE) ranged from 64.78 μg/m^3 to 317.73 μg/m^3, with a mean over all of the stations of 181.28
358 μg/m^3. The relatively large values of the MB, ME and RMSE are mainly attributed to the fact that no other aerosol
359 emissions were considered in the simulations other than dust, while the surface PM_{10} concentration at the monitoring
360 stations is influenced by aerosols emitted from other sources, such as anthropogenic emissions. The correlation
361 coefficient (r) ranged from 0.59 to 0.87, with an average for all of the stations of 0.70. The comparisons between the
362 observed and simulated surface PM_{10} concentration indicates that the model is capable of reproducing the surface dust
363 concentration reasonably during dust events over East Asia.

© Author(s) 2017. CC BY 4.0 License.

364

365 **5.1.2 AOD time series**

366 To examine the performance of the model in reproducing the column sum of dust in the atmosphere, the simulated
367 AOD values were compared with observations measured at two AERONET sites during the simulation period, as
368 shown in Figure 4.

369 The site at Dalanzadgad (Figure 4a) is located in Mongolia to the north of the Gobi Desert. Despite the fact that the
370 simulated AOD was overestimated at the end of March and in mid-April compared to the observed values, the trend
371 and magnitude of the AOD time series at Dalanzadgad was reasonably reproduced by the model during the simulation
372 period.

373 SACOL (Figure 4b) is a site located in Lanzhou, Gansu Province, which is a typical downwind area for dust in China.
374 Apart from the overestimation on April 23, the model showed a good performance in reproducing the time series of
375 AOD at SACOL during the entire simulation period, with the trend and magnitude of AOD well captured.

376

377 **5.1.3 Satellite-observational AOD**

378 The spatial distribution of mean simulated AOD during the simulation period was also compared with observed values
379 from MODIS and MISR products. The AOD observed by MODIS showed high values at the dust source region in
380 both March and April of 2012, as shown in Figures 5a and b. The region with high AOD values in the west part of the
381 circled area is the Taklimakan Desert, and the region with relatively lower AOD in the east part of the circled area is
382 the Gobi Desert. The mean observed AOD over the Gobi Desert was lower than that over the Taklimakan Desert in
383 both March and April, and the mean observed AOD was higher in April than in March over both dust source areas.
384 The spatial patterns of AOD observed by MISR are similar to MODIS, with comparable values over the Gobi Desert,
385 but significantly lower values over the Taklimakan Desert in both March and April (Figure 5c and d).

386 The spatial patterns for the mean simulated AOD were similar to the observed values for the observations in both
387 months, as shown in Figures 5e and f. The model shows a good capability in capturing the spatial characteristics of
388 the AOD, as well as the trend in AOD from March to April over the dust source areas. For example, the mean AOD

© Author(s) 2017. CC BY 4.0 License.

389 in the southern part of the Taklimakan Desert was higher than that in the northern part in March, and the mean AOD
390 showed an increase from March to April over the Gobi Desert, both of which were captured by the model. The values
391 of the mean simulated AOD over the Gobi Desert are comparable to the observational values from both MODIS and
392 MISR, but the mean simulated AOD over the Taklimakan Desert are between the values of the MISR observations
393 and the MODIS observations.

394 In summary, it was demonstrated that the dust emissions simulated by WRF-Chem are reliable for further analysis by
395 the comparison between the simulation results and the observations for surface PM_{10} concentrations, as well as the
396 temporal and spatial distributions of AOD values.

397

398 **5.2 Atmospheric ice water content**

399 Dust particles are effective ice nuclei and play an important role in ice nucleation in the atmosphere under appropriate
400 conditions. With the large number of ice nuclei served by dust particles emitted into the atmosphere, an increase in
401 the number of ice crystals is expected in the results from DUST compared with those from CTRL, after taking into
402 account the effects of dust particles in the GOCART–Thompson microphysics scheme, as the ice nucleation process
403 is triggered by dust particles at appropriate temperature and relative humidity, as shown by the overall comparison
404 between the simulated cloud ice mixing ratio and ice crystal number concentration at each simulated data point (at
405 all model grids at hourly intervals) from CTRL and DUST during the entire simulation period in Figure 6.

406 As expected, the model produces a much higher cloud ice mixing ratio (Figure 6a) and ice crystal number
407 concentration (Figure 6b) in DUST. The simulated cloud ice mixing ratio produced in CTRL is lower than 2 μg/kg at
408 most data points during the simulation period, whereas the data points with simulated ice mixing ratio higher than 2
409 μg/kg are substantially increased in the output of DUST. Similarly, the simulated ice crystal number concentration
410 produced in CTRL is lower than 0.5×10^6 #/kg at most data points during the simulation period, by contrast, the
411 simulated ice crystal number concentration number concentration is higher than 0.5×10^6 #/kg at over a half of total
412 data points in DUST. The substantial increase of simulated cloud ice mixing ratio and ice crystal number concentration
413 indicates that the enhancement of ice nucleation process induced by dust is successfully reproduced by the newly-
414 implemented GOCART-Thompson microphysics scheme during the simulation period.

© Author(s) 2017. CC BY 4.0 License.

415 The spatial distributions of the simulated ice water path and ice crystal number density from CTRL and DUST in
416 Figure 7 further demonstrate the spatial pattern of the enhancement in cloud ice due to dust over East Asia. The ice
417 water path produced by CTRL was lower than 1 g/m^2 over the entire East Asia Region (Figure 7a). After considering
418 the effect of dust in the ice nucleation process, the ice water path produced by DUST increased substantially over the
419 entire region, especially over dust sources and downwind areas, with values as high as 10 g/m^2 (Figure 7b and c). The
420 ice water path was increased by one order of magnitude as a result of the effect of dust particles serving as ice nuclei
421 in the atmosphere. As shown in Figures 7d–f, the spatial pattern for the enhancement of ice crystal number density
422 over East Asia was similar with that for the ice water path. The ice crystal number density was increased by one order
423 of magnitude over vast areas of East Asia upon considering the effect of dust in the ice nucleation process in the
424 simulation.

425

426 **5.2.1 Ice water path**

427 The mean simulated ice water path during the simulation period was compared to the observed ice water path retrieved
428 from the MODIS products, as shown in Figure 8. MODIS observed ice water content in the atmosphere including
429 precipitating ice, such as snow and graupel, and cloud ice, which remains suspended in the upper troposphere and
430 lower stratosphere (Eliasson et al., 2011). Therefore, the simulated ice water path for comparison with the observations
431 also contained all of the precipitable ice variables output by the model, including snow, graupel, and cloud ice.

432 In Figure 8a, high ice water paths were observed at three areas over East Asia, as indicated by the red rectangles: in
433 the west part of the simulation domain containing the Taklimakan Desert and the Tibetan Plateau, South China, and
434 the area from Northeast China to Japan, with the highest values located at the south side of the Himalayas, and in
435 South China.

436 The simulated ice water paths produced by CTRL and DUST, as shown in Figures 7b and c, have nearly identical
437 spatial patterns and magnitudes. Typically, the ratio of cloud ice to the total column of ice particles in model outputs
438 is on the order of 0.1 to 0.3 (Waliser et al., 2009), and the effect of dust in ice nucleation leads to a direct enhancement
439 in cloud ice in the simulation, but not precipitable ice; therefore, the enhancement in cloud ice induced by dust is
440 concealed in the ice water path containing all atmospheric ice water, including precipitating ice and cloud ice.

© Author(s) 2017. CC BY 4.0 License.

441 Nevertheless, in the results of both CTRL and DUST, the model produced a high ice water path over West China, and
442 the concentrated ice water path from Northeast China to Japan was also captured, albeit with a different pattern.
443 However, the high ice water path over South China was missed in the results of both CTRL and DUST. This might
444 be attributable to the following reasons. Firstly, the temperature in the upper troposphere produced by the model might
445 be too high over this area for super-cooled water droplets freezing into ice particles. Secondly, the high ice water path
446 observed over South China is mainly due to strong convection motions that occur frequently over this area during
447 spring. The moisture convection produced by the model might be too weak to transport sufficient water vapor into the
448 upper troposphere, leading to an overestimation of the ice water path over this area.

449 The ice water path over areas other than the aforementioned regions in the simulation domain was underestimated by
450 the model; however, it can be seen that the ice water path produced in DUST was higher than that produced in CTRL
451 over the dust source region and Southwest Pacific, which is more consistent with the observed results, suggesting that
452 the model exhibits a better performance in reproducing ice water path over East Asia when the effect of dust is taken
453 into account in the simulation.

454

455 **5.2.2 Ice water content during dust events**

456 The vertical profile of the simulated ice water content was also compared with the observation from CALIPSO during
457 dust events. As mentioned in section 5.1, a total of four dust events occurred during the simulation period, lasting
458 from March 18 to 25, March 30 to April 7, April 9 to 19, and April 22 to 28, 2012. As shown in Figures 9 and 11, the
459 simulated vertical profiles of the ice water content during each dust events were compared with observations measured
460 at 06 UTC on March 21, 18 UTC on April 1, 18 UTC on April 9, and 05 UTC on April 23, 2012, when the orbit of
461 the satellite passed over East Asia.

462 Unlike the MODIS ice water path, CALIPSO measures the global distribution of aerosol and cloud properties by
463 LIDAR, which uses a laser to generate visible light with a wavelength of 1 μm or less to detect small particles or
464 droplets in the atmosphere. Therefore, CALIPSO instruments are more sensitive to tenuous ice clouds and liquid
465 clouds composed of small particles or droplets, which are invisible to instruments using signals of near-infrared or
466 infrared wavelength to detect clouds. Moreover, the LIDAR signal is attenuated rapidly in optically dense clouds that

© Author(s) 2017. CC BY 4.0 License.

the infrared or near-infrared signals can easily penetrate(Winker et al., 2010). As a result, the CALIPSO observations of ice water content are mostly points where the temperatures is lower than −40 °C and the altitude is greater than 6 km poleward to 12 km equatorward, and mostly those without precipitating ice. Given the above considerations, the simulated ice water content profiles compared with the CALIPSO observations are referred to as only cloud ice in this section.

The simulated dust load over East Asia at 06 UTC on March 21, 2012 is shown in Figure 9a, in which the dust covered vast areas from West to East China between 35°N and 45°N, and the orbit of the satellite passed through the area with heavy dust load at around 100°E. Along the satellite orbit, the abundant dust particles were transported to as high as 10 km aloft (Figure 9c). At this time, a high concentration of ice water content was observed along the satellite orbit at an altitude of around 10 km between 30°N and 45°N (Figure 9e). The simulation result from CTRL (Figure 9g) shows that the model produces some ice cloud at altitude of 9–10 km between 35°N and 45°N, but with much lower ice water content compared to the observations. Nevertheless, by applying the GOCART–Thompson microphysics scheme, the effect of dust in ice nucleation process was considered in DUST, leading to a much higher ice water content at altitude of 9–10 km between 35°N and 45°N (Figure 9i), which is much more consistent with the observations. The comparison between the simulation results from CTRL and DUST indicates that the high ice water content observed by the satellite between 30°N and 35°N might be unrelated to microphysical processes, but instead due to strong convective motions over South China.

On April 1, 2012, Central to East China was covered by a thick dust plume, and the orbit of the satellite passed through areas with heavy dust load between 25°N and 43°N along 120°E at 18 UTC (Figure 9b). Dust particles were distributed vertically from the surface to over 8 km along the satellite orbit (Figure 9d). A band of high ice water content was observed by the satellite at altitude of 5 km to 10 km between 33°N and 44°N (Figure 9f), which was barely reproduced in the results of the CTRL run without dust. In contrast, the observed band of high ice water content was reproduced by the model in DUST with much more consistent location and magnitude (Figure 9j).

At 18 UTC on April 9, 2012, the satellite was scanning the east coast of China, which was covered by a thick dust plume between 35°N and 45°N (Figure 10a), with dust particles lifted up to 10 km above the surface (Figure 10c). High concentration of ice water content was observed by the satellite at altitude from 5 km to 11 km between 30°N and 45°N (Figure 10e). In this case, the model reproduced the high concentration of ice water content at the observed

© Author(s) 2017. CC BY 4.0 License.

location in the results from both CTRL and DUST, although the ice water content was significantly underestimated in the results from CTRL (Figure 10g), while it was well reproduced in the results from DUST (Figure 10j).

Similar to the previous cases, the satellite was scanning along east coast of China at 05 UTC on April 23, 2012, when a dust plume was arriving in East China and affecting areas between 35°N and 45°N (Figure 10b), and dust particles were distributed vertically from the surface to 10 km along the scanning track of the satellite (Figure 10d). Along the orbit of the satellite, two bands with high ice water content were observed at altitudes between 5 km and 12 km, one is located between 30°N and 37°N, and the other is located between 40°N and 45°N (Figure 10f). In the results from CTRL, the model reproduced the bands of high ice water content at the correct locations, but with substantially lower values (Figure 10h); however, upon taking into account the effect of dust in the GOCART-Thompson microphysics scheme, the bands of high ice water content were well reproduced by the model, with much more consistent values (Figure 10-j).

By comparing the satellite-observational and simulated vertical profiles of ice water content during the various dust events, it was demonstrated that the newly-implemented GOCART–Thompson microphysics scheme reproduces the enhancement of ice water content clouds in the mid- to upper troposphere by taking in to account the effect of dust in the ice nucleation process, which substantially improves the simulation of cloud ice.

5.2.3 Mean vertical profiles of ice water content

The mean profiles of the observed ice water content, as well as the simulated ice water content from CTRL and DUST for the four dust events discussed in Section 5.2.2, are shown in Figure 11. Note that the "mean profile" of ice water content is the average over the available data points for the ice water content along the orbit of the satellite between 30°N to 45°N for each of the dust events shown in Figures 9 and 11.

The black lines in Figure 11 represent the mean profile of the observed ice water content, and the blue and red lines represent the mean profiles of the simulated ice water content from CTRL and DUST, respectively.

Compared with the results from CTRL, the simulation for the vertical profile of the ice water content was substantially improved in DUST for each dust event, with the enhancement of the ice nucleation process well captured by the

© Author(s) 2017. CC BY 4.0 License.

519 GOCART-Thompson microphysics scheme, although there were still discrepancies between observations and the
520 simulation results from DUST.

521 For the cases on March 21 and April 1, the peaks of ice water content were observed at 9.5 km and 8 km, respectively,
522 whereas the simulated peak of ice water content were located at 8 km and 7.5 km, respectively, with lower peak values.
523 The lower peak value for the case on March 21 was due to the missing of the high ice water content observed between
524 30°N to 45°N in the simulation results (Figure 9e and i), while the lower peak value for the case on April 1 was due
525 to the underestimation of the ice water content around 35°N (Figure 9f and j). The locations of the peaks of simulated
526 ice water content for the cases on April 9 and April 23 are more consistent with the observed peaks, but still possessed
527 lower values due to the missing or underestimation of high ice water content in the observations.

528

529 **5.3 Sensitivity test and discussion**

530 As discussed in Section 5.2.3, the simulation of cloud ice is greatly improved by considering the enhancement of ice
531 nucleation process induced by dust, which is well captured by the GOCART–Thompson microphysics scheme.
532 However, the ice water content is still underestimated by the model during dust events. To determine the reason for
533 this limitation, numerical experiments were performed to investigate the sensitivity of simulated ice water content to
534 the parameters for the ice nucleation parameterization in the GOCART–Thompson microphysics scheme.

535

536 **5.3.1 Calibration factor c_f**

537 The calibration factor c_f is an empirical tuning coefficient derived from observational data from field and laboratory
538 experiments. It ranges from 1 to 6, and recommended to be 3 (DeMott et al., 2015), which was applied in the previous
539 simulations. An experiment was conducted to investigate the sensitivity of the simulated ice water content to c_f values
540 ranging from 3 to 6.

541 The mean profiles of ice water content from simulation results were compared with the CALIPSO observations for
542 the dust events discussed in Section 5.2.2 and 5.2.3, as shown in Figure 12. For the cases on March 21 and April 1,
543 changing c_f did not result in an increase of ice water content; instead, the simulated ice water content remained

© Author(s) 2017. CC BY 4.0 License.

consistent for c_f values varying from 3 to 6. As ice nucleation occurs only in a super-saturated atmosphere with respect to water vapor, an upper limit was set in the Thompson microphysics scheme, in that once the coagulation makes the relative humidity in the atmosphere lower than the threshold relative humidity, which was set to 105% in the simulations, the ice nucleation process is terminated. The consistency in simulated ice water content with increasing c_f indicates that the ice water content reaches the upper limit with all the available water vapor coagulated into ice crystals when c_f is equal to 3, lowering the relative humidity in the atmospheric column to below 105% for these two cases.

For the case on April 9, the simulated ice water content increased between 6 km and 9 km and matched the observed profile better when c_f was equal to 4 and 5; however, when c_f was set to 6, the simulated ice water content was lower than that obtained with c_f values of 4 or 5, although it matched the observed profile better than that produced with a c_f of 3.

For the case on April 23, two peaks were observed in the profile of simulated ice water content, located at 7 km and 10 km. The simulated ice water content remained unchanged with c_f values varying from 3 to 6 for the peak at 10 km, but increased upon changing the c_f from 3 to 4, and remained the same upon changing the c_f from 5 and 6 for the peak at 7 km. In this case, the peak of the simulated ice water content at 7 km should correspond to the observed peak between 6 km to 8 km, which was slightly overestimated by the model, and increasing the c_f resulted in even larger overestimation of this peak.

Given the above discussion, increasing the calibration factor c_f from 3 to 6 does not necessarily lead to a significant variation in the simulated ice water content during dust events, and the model achieves a relatively better performance in reproducing the profile of ice water content when the c_f is set to 3 or 4.

5.3.2 Threshold RH_i

In this study, the threshold RH_i that triggers the ice nucleation process in the simulation was set to be 105%. Since the ice water content is underestimated in the simulations, a sensitivity experiment was carried out to investigate the response of simulated ice water content to a lower threshold RH_i (100%).

© Author(s) 2017. CC BY 4.0 License.

569 The mean profiles of ice water content from the simulation results were compared with the CALIPSO observations
570 for the aforementioned dust events, as shown in Figure 13. With the threshold RH_i lowered to 100%, the simulated
571 ice water content showed an increase throughout the vertical profile, with the most significant increase at the peak,
572 suggesting more consistency with the observations for all of the dust events, except the one on April 1. In the case on
573 April 1, the simulated ice water content increased at lower layers than the peak, but slightly decreased right at the peak
574 upon lowering the threshold relative humidity with respect to ice to 100% for the case. Overall, the simulation of ice
575 water content during dust events was significantly improved by lowering the threshold RH_i from 105% to 100%.

576

577 **6 Conclusions**

578 The GOCART–Thompson scheme was implemented into WRF-Chem to couple the GOCART dust model and the
579 aerosol-aware Thompson microphysics scheme. By applying this microphysics scheme, the effect of dust on the ice
580 nucleation process by serving as ice nuclei in the atmosphere can be quantified and evaluated by the model
581 simultaneously with dust simulation. Numerical experiments, including a control run without dust and a test run with
582 dust, were then carried out to evaluate the performance of the GOCART–Thompson microphysics scheme in
583 simulating the effect of dust on the content of cloud ice over East Asia during a typical dust-intensive period, by
584 comparing the simulation results with various observations.

585 Based on the GOCART aerosol model the model reproduces dust emission reasonably well, by capturing the trend
586 and magnitude of surface PM_{10} concentration at various environmental monitoring stations and the AOD at two
587 AERONET sites. The spatial patterns of the mean AOD over East Asia during the simulation period were also
588 consistent with satellite observations.

589 The effect of dust on the ice nucleation process by serving as ice nuclei was then quantified and evaluated in the
590 GOCART–Thompson microphysics scheme. Upon considering the effect of dust in the simulation, the simulated ice
591 water mixing ratio and ice crystal number concentration over East Asia were one order of magnitude higher than those
592 simulated without dust, with the most significant enhancements located over dust source regions and downwind areas.

593 By comparing the mean simulated ice water path over East Asia during the simulation period with MODIS
594 observations, it was demonstrated that the ice water path including cloud ice and precipitating ice is reasonably

© Author(s) 2017. CC BY 4.0 License.

595 reproduced by the model over most areas of East Asia, with the results from the simulation run with dust more
596 consistent with the observations.

597 Comparison between the vertical profiles of the satellite-observed and simulated ice water content during various dust
598 events and the entire simulation period further indicated that the enhancement of cloud ice induced by abundant dust
599 particles serving as ice nuclei is well captured by the GOCART–Thompson microphysics scheme, with the results
600 from the simulation with dust much more consistent with the satellite–observations.

601 Sensitivity experiments revealed that the simulated ice water content is not very sensitive to the calibration factor in
602 the DeMott2015 ice nucleation scheme, but the model delivered a slight better performance in reproducing the ice
603 water content when the calibration factor was set to 3 or 4. However, the simulated ice water content is sensitive to
604 the threshold RH_i to trigger the ice nucleation process in the model, and the simulation of ice water content is
605 significantly improved upon lowering the threshold RH_i from 105% to 100%.

606

607 **Acknowledgement**. We would like to acknowledge the provision of the MODIS and the MISR observations by the
608 Ministry of Environmental Protection Data Center, U.S. National Center for Atmospheric Research (NCAR), and the
609 CALIPSO data by the U.S. National Aeronautics and Space Administration (NASA) Data Center. We thank the
610 principal investigators and their staff for establishing and maintaining the two AERONET sites used in this study. The
611 AERONET data were obtained freely from the AERONET program website (https://aeronet.gsfc.nasa.gov/). We
612 appreciate the assistance of the Hong Kong Observatory (HKO), which provided the meteorological data. Lin Su
613 would like to thank Dr. Georg Grell, Dr. Stuart McKeen, and Dr. Ravan Ahmandov from the Earth System Research
614 Laboratory, U.S. National Oceanic and Atmospheric Administration for insightful discussions. Other data used this
615 paper are properly cited and referred to in the reference list. All data shown in the results are available upon request.
616 This work was supported by NSFC/RGC Grant N_HKUST631/05,
617 NSFC-FD Grant U1033001, and the RGC Grant 16303416.

618

© Author(s) 2017. CC BY 4.0 License.

References

Ashrafi, K., Motlagh, M. S., and Neyestani, S. E.: Dust storms modeling and their impacts on air quality and radiation budget over Iran using WRF-Chem, Air Quality, Atmosphere & Health, 1-18, 2017.

Atkinson, J. D., Murray, B. J., Woodhouse, M. T., Whale, T. F., Baustian, K. J., Carslaw, K. S., Dobbie, S., O'sullivan, D., and Malkin, T. L.: The importance of feldspar for ice nucleation by mineral dust inmixed-phase clouds, Nature, 498, 355, 2013.

Baró, R., Jiménez-Guerrero, P., Balzarini, A., Curci, G., Forkel, R., Grell, G., Hirtl, M., Honzak, L., Langer, M., and Pérez, J. L.: Sensitivity analysis of the microphysics scheme in WRF-Chem contributions to AQMEII phase 2, Atmospheric Environment, 115, 620-629, 2015.

Bi, J., Huang, J., Fu, Q., Ge, J., Shi, J., Zhou, T., and Zhang, W.: Field measurement of clear-sky solar irradiance in Badain Jaran Desert of Northwestern China, Journal of Quantitative Spectroscopy and Radiative Transfer, 122, 194-207, 2013.

Bigg, E.: The formation of atmospheric ice crystals by the freezing of droplets, Quarterly Journal of the Royal Meteorological Society, 79, 510-519, 1953.

Chapman, E. G., Gustafson Jr, W., Easter, R. C., Barnard, J. C., Ghan, S. J., Pekour, M. S., and Fast, J. D.: Coupling aerosol-cloud-radiative processes in the WRF-Chem model: Investigating the radiative impact of elevated point sources, Atmospheric Chemistry and Physics, 9, 945-964, 2009.

Chen, S., Zhao, C., Qian, Y., Leung, L. R., Huang, J., Huang, Z., Bi, J., Zhang, W., Shi, J., and Yang, L.: Regional modeling of dust mass balance and radiative forcing over East Asia using WRF-Chem, Aeolian Research, 15, 15-30, 2014.

Chiao, S., Jenkins, G., Ulanowski, Z., and Smith, H.: Improved understanding of the vertical distribution of simulated dust distribution in the Saharan Air Layer during the ICE-D field campaign with the WRF-CHEM model, 2016.

Chin, M., Rood, R. B., Lin, S.-J., Müller, J.-F., and Thompson, A. M.: Atmospheric sulfur cycle simulated in the global model GOCART: Model description and global properties, 2000.

Cooper, W. A.: Ice initiation in natural clouds, in: Precipitation Enhancement—A Scientific Challenge, Springer, 29-32, 1986.

DeMott, P. J., Sassen, K., Poellot, M. R., Baumgardner, D., Rogers, D. C., Brooks, S. D., Prenni, A. J., and Kreidenweis, S. M.: African dust aerosols as atmospheric ice nuclei, Geophysical Research Letters, 30, 2003.

© Author(s) 2017. CC BY 4.0 License.

647 DeMott, P. J., Prenni, A. J., Liu, X., Kreidenweis, S. M., Petters, M. D., Twohy, C. H., Richardson, M., Eidhammer, T.,
648 and Rogers, D.: Predicting global atmospheric ice nuclei distributions and their impacts on climate, Proceedings of
649 the National Academy of Sciences, 107, 11217-11222, 2010.
650 DeMott, P. J., Prenni, A. J., McMeeking, G. R., Sullivan, R. C., Petters, M. D., Tobo, Y., Niemand, M., Möhler, O.,
651 Snider, J. R., and Wang, Z.: Integrating laboratory and field data to quantify the immersion freezing ice nucleation
652 activity of mineral dust particles, Atmospheric Chemistry and Physics, 15, 393-409, 2015.
653 Diner, D. J., Barge, L. M., Bruegge, C. J., Chrien, T. G., Conel, J. E., Eastwood, M. L., Garcia, J. D., Hernandez, M. A.,
654 Kurzweil, C. G., and Ledeboer, W. C.: The Airborne Multi-angle Imaging SpectroRadiometer (AirMISR): instrument
655 description and first results, IEEE Transactions on Geoscience and Remote Sensing, 36, 1339-1349, 1998.
656 Eliasson, S., Buehler, S., Milz, M., Eriksson, P., and John, V.: Assessing observed and modelled spatial distributions of
657 ice water path using satellite data, Atmospheric Chemistry and Physics, 11, 375-391, 2011.
658 Flaounas, E., Kotroni, V., Lagouvardos, K., Klose, M., Flamant, C., and Giannaros, T. M.: Sensitivity of the WRF-Chem
659 (V3. 6.1) model to different dust emission parametrisation: assessment in the broader Mediterranean region,
660 Geoscientific Model Development, 10, 2925, 2017.
661 Gao, B.-C., and Kaufman, Y. J.: The MODIS near-IR water vapor algorithm, Algorithm Theoretical Basis Document,
662 ATBD-MOD, 5, 1998.
663 Ge, J., Su, J., Ackerman, T., Fu, Q., Huang, J., and Shi, J.: Dust aerosol optical properties retrieval and radiative forcing
664 over northwestern China during the 2008 China-US joint field experiment, Journal of Geophysical Research:
665 Atmospheres, 115, 2010.
666 Ginoux, P., Chin, M., Tegen, I., Prospero, J. M., Holben, B., Dubovik, O., and Lin, S. J.: Sources and distributions of dust
667 aerosols simulated with the GOCART model, Journal of Geophysical Research: Atmospheres, 106, 20255-20273,
668 2001.
669 Ginoux, P., Prospero, J. M., Torres, O., and Chin, M.: Long-term simulation of global dust distribution with the GOCART
670 model: correlation with North Atlantic Oscillation, Environmental Modelling & Software, 19, 113-128, 2004.
671 Grell, G., Peckham, S., Fast, J., Singh, B., Easter, R., Gustafson, W., Rasch, P., Wolters, S., Barth, M., and Pfister, G.:
672 WRF-Chem V3. 5: A summary of status and updates, EGU General Assembly Conference Abstracts, 2013, 11332.
673 Grell, G. A., and Freitas, S. R.: A scale and aerosol aware stochastic convective parameterization for weather and air
674 quality modeling, Atmos. Chem. Phys, 14, 5233-5250, 2014.

© Author(s) 2017. CC BY 4.0 License.

675 Hansen, J., Sato, M., and Ruedy, R.: Radiative forcing and climate response, Journal of Geophysical Research:
676 Atmospheres, 102, 6831-6864, 1997.
677 Hartmann, D., Tank, A., and Rusticucci, M.: IPCC fifth assessment report, climate change 2013: The physical science
678 basis, IPCC AR5, 31-39, 2013.
679 Holben, B., Tanre, D., Smirnov, A., Eck, T., Slutsker, I., Abuhassan, N., Newcomb, W., Schafer, J., Chatenet, B., and
680 Lavenu, F.: An emerging ground-based aerosol climatology: Aerosol optical depth from AERONET, Journal of
681 Geophysical Research: Atmospheres, 106, 12067-12097, 2001.
682 Hoose, C., Lohmann, U., Erdin, R., and Tegen, I.: The global influence of dust mineralogical composition on
683 heterogeneous ice nucleation in mixed-phase clouds, Environmental Research Letters, 3, 025003, 2008.
684 Hsu, N. C., Tsay, S.-C., King, M. D., and Herman, J. R.: Deep blue retrievals of Asian aerosol properties during ACE-
685 Asia, IEEE Transactions on Geoscience and Remote Sensing, 44, 3180-3195, 2006.
686 Huang, J., Fu, Q., Su, J., Tang, Q., Minnis, P., Hu, Y., Yi, Y., and Zhao, Q.: Taklimakan dust aerosol radiative heating
687 derived from CALIPSO observations using the Fu-Liou radiation model with CERES constraints, Atmospheric
688 Chemistry and Physics, 9, 4011-4021, 2009.
689 Huang, J.: Emission, transport, and radiative effects of mineral dust from the Taklimakan and Gobi deserts: comparison
690 of measurements and model results, Atmos. Chem. Phys, 1680, 7324, 2017.
691 Iacono, M. J., Delamere, J. S., Mlawer, E. J., Shephard, M. W., Clough, S. A., and Collins, W. D.: Radiative forcing by
692 long-lived greenhouse gases: Calculations with the AER radiative transfer models, Journal of Geophysical Research:
693 Atmospheres, 113, 2008.
694 Janjić, Z. I.: The step-mountain eta coordinate model: Further developments of the convection, viscous sublayer, and
695 turbulence closure schemes, Monthly Weather Review, 122, 927-945, 1994.
696 Janjić, Z. I.: Nonsingular implementation of the Mellor–Yamada level 2.5 scheme in the NCEP Meso model, NCEP office
697 note, 437, 61, 2002.
698 Kang, J. Y., Yoon, S. C., Shao, Y., and Kim, S. W.: Comparison of vertical dust flux by implementing three dust emission
699 schemes in WRF/Chem, Journal of Geophysical Research: Atmospheres, 116, 2011.
700 Karydis, V., Kumar, P., Barahona, D., Sokolik, I., and Nenes, A.: On the effect of dust particles on global cloud
701 condensation nuclei and cloud droplet number, Journal of Geophysical Research: Atmospheres, 116, 2011.

© Author(s) 2017. CC BY 4.0 License.

Kaufman, Y., Tanré, D., Remer, L. A., Vermote, E., Chu, A., and Holben, B.: Operational remote sensing of tropospheric aerosol over land from EOS moderate resolution imaging spectroradiometer, Journal of Geophysical Research: Atmospheres, 102, 17051-17067, 1997.

Koehler, K., Kreidenweis, S., DeMott, P., Petters, M., Prenni, A., and Möhler, O.: Laboratory investigations of the impact of mineral dust aerosol on cold cloud formation, Atmospheric Chemistry and Physics, 10, 11955-11968, 2010.

Kumar, R., Barth, M., Pfister, G., Naja, M., and Brasseur, G.: WRF-Chem simulations of a typical pre-monsoon dust storm in northern India: influences on aerosol optical properties and radiation budget, Atmospheric Chemistry and Physics, 14, 2431-2446, 2014.

Lacis, A.: Climate forcing, climate sensitivity, and climate response: A radiative modeling perspective on atmospheric aerosols, Aerosol forcing of climate, 11-42, 1995.

Liu, Huang, J., Shi, G., Takamura, T., Khatri, P., Bi, J., Shi, J., Wang, T., Wang, X., and Zhang, B.: Aerosol optical properties and radiative effect determined from sky-radiometer over Loess Plateau of Northwest China, Atmospheric Chemistry and Physics, 11, 11455-11463, 2011a.

Liu, Zheng, Y., Li, Z., Flynn, C., Welton, E. J., and Cribb, M.: Transport, vertical structure and radiative properties of dust events in southeast China determined from ground and space sensors, Atmospheric environment, 45, 6469-6480, 2011b.

Lohmann, U., and Diehl, K.: Sensitivity studies of the importance of dust ice nuclei for the indirect aerosol effect on stratiform mixed-phase clouds, Journal of the Atmospheric Sciences, 63, 968-982, 2006.

Mallet, M., Tulet, P., Serça, D., Solmon, F., Dubovik, O., Pelon, J., Pont, V., and Thouron, O.: Impact of dust aerosols on the radiative budget, surface heat fluxes, heating rate profiles and convective activity over West Africa during March 2006, Atmospheric Chemistry and Physics, 9, 7143-7160, 2009.

Martonchik, J., Diner, D., Kahn, R., Gaitley, B., and Holben, B.: Comparison of MISR and AERONET aerosol optical depths over desert sites, Geophysical Research Letters, 31, 2004.

Miller, R., Tegen, I., and Perlwitz, J.: Surface radiative forcing by soil dust aerosols and the hydrologic cycle, Journal of Geophysical Research: Atmospheres, 109, 2004.

Mlawer, E. J., Taubman, S. J., Brown, P. D., Iacono, M. J., and Clough, S. A.: Radiative transfer for inhomogeneous atmospheres: RRTM, a validated correlated-k model for the longwave, Journal of Geophysical Research: Atmospheres, 102, 16663-16682, 1997.

© Author(s) 2017. CC BY 4.0 License.

730 Nabat, P., Somot, S., Mallet, M., Michou, M., Sevault, F., Driouech, F., Meloni, D., Di Sarra, A., Di Biagio, C., and
731 Formenti, P.: Dust aerosol radiative effects during summer 2012 simulated with a coupled regional aerosol–
732 atmosphere–ocean model over the Mediterranean, Atmospheric Chemistry and Physics, 15, 3303-3326, 2015a.
733 Nabat, P., Somot, S., Mallet, M., Sevault, F., Chiacchio, M., and Wild, M.: Direct and semi-direct aerosol radiative effect
734 on the Mediterranean climate variability using a coupled regional climate system model, Climate dynamics, 44, 1127-
735 1155, 2015b.
736 Perlwitz, J., and Miller, R. L.: Cloud cover increase with increasing aerosol absorptivity: A counterexample to the
737 conventional semidirect aerosol effect, Journal of Geophysical Research: Atmospheres, 115, 2010.
738 Phillips, V. T., DeMott, P. J., and Andronache, C.: An empirical parameterization of heterogeneous ice nucleation for
739 multiple chemical species of aerosol, Journal of the atmospheric sciences, 65, 2757-2783, 2008.
740 Rizza, U., Barnaba, F., Miglietta, M. M., Mangia, C., Di Liberto, L., Dionisi, D., Costabile, F., Grasso, F., and Gobbi, G.
741 P.: WRF-Chem model simulations of a dust outbreak over the central Mediterranean and comparison with multi-
742 sensor desert dust observations, Atmospheric Chemistry and Physics, 17, 93, 2017.
743 Seigel, R., Van Den Heever, S., and Saleeby, S.: Mineral dust indirect effects and cloud radiative feedbacks of a simulated
744 idealized nocturnal squall line, Atmospheric Chemistry and Physics, 13, 4467-4485, 2013.
745 Shao: A model for mineral dust emission, Journal of Geophysical Research: Atmospheres, 106, 20239-20254, 2001.
746 Shao: Simplification of a dust emission scheme and comparison with data, Journal of Geophysical Research: Atmospheres,
747 109, 2004.
748 Shao, Ishizuka, M., Mikami, M., and Leys, J.: Parameterization of size-resolved dust emission and validation with
749 measurements, Journal of Geophysical Research: Atmospheres, 116, 2011.
750 Soil Survey Staff: Soil survey manual, 1993.
751 Solomos, S., Kallos, G., Kushta, J., Astitha, M., Tremback, C., Nenes, A., and Levin, Z.: An integrated modeling study
752 on the effects of mineral dust and sea salt particles on clouds and precipitation, Atmospheric Chemistry and Physics,
753 11, 873-892, 2011.
754 Su, L., and Fung, J. C.: Sensitivities of WRF-Chem to dust emission schemes and land surface properties in simulating
755 dust cycles during springtime over East Asia, Journal of Geophysical Research: Atmospheres, 120, 2015.

© Author(s) 2017. CC BY 4.0 License.

Tesfaye, M., Tsidu, G. M., Botai, J., and Sivakumar, V.: Mineral dust aerosol distributions, its direct and semi-direct effects over South Africa based on regional climate model simulation, Journal of Arid Environments, 114, 22-40, 2015.

Textor, C., Schulz, M., Guibert, S., Kinne, S., Balkanski, Y., Bauer, S., Berntsen, T., Berglen, T., Boucher, O., and Chin, M.: Analysis and quantification of the diversities of aerosol life cycles within AeroCom, Atmospheric Chemistry and Physics, 6, 1777-1813, 2006.

Thompson, G., and Eidhammer, T.: A study of aerosol impacts on clouds and precipitation development in a large winter cyclone, Journal of the Atmospheric Sciences, 71, 3636-3658, 2014.

Twohy, C. H., Kreidenweis, S. M., Eidhammer, T., Browell, E. V., Heymsfield, A. J., Bansemer, A. R., Anderson, B. E., Chen, G., Ismail, S., and DeMott, P. J.: Saharan dust particles nucleate droplets in eastern Atlantic clouds, Geophysical Research Letters, 36, 2009.

Vaughan, M. A., Young, S. A., Winker, D. M., Powell, K. A., Omar, A. H., Liu, Z., Hu, Y., and Hostetler, C. A.: Fully automated analysis of space-based lidar data: An overview of the CALIPSO retrieval algorithms and data products, Remote Sensing, 2004, 16-30.

Waliser, D. E., Li, J. L. F., Woods, C. P., Austin, R. T., Bacmeister, J., Chern, J., Del Genio, A., Jiang, J. H., Kuang, Z., and Meng, H.: Cloud ice: A climate model challenge with signs and expectations of progress, Journal of Geophysical Research: Atmospheres, 114, 2009.

Wesely, M.: Parameterization of surface resistances to gaseous dry deposition in regional-scale numerical models, Atmospheric Environment (1967), 23, 1293-1304, 1989.

Winker, Pelon, J., Coakley Jr, J., Ackerman, S., Charlson, R., Colarco, P., Flamant, P., Fu, Q., Hoff, R., and Kittaka, C.: The CALIPSO mission: A global 3D view of aerosols and clouds, Bulletin of the American Meteorological Society, 91, 1211-1229, 2010.

Winker, D. M., Vaughan, M. A., Omar, A., Hu, Y., Powell, K. A., Liu, Z., Hunt, W. H., and Young, S. A.: Overview of the CALIPSO mission and CALIOP data processing algorithms, Journal of Atmospheric and Oceanic Technology, 26, 2310-2323, 2009.

Zhang, C., Wang, M., Morrison, H., Somerville, R. C., Zhang, K., Liu, X., and Li, J. L. F.: Investigating ice nucleation in cirrus clouds with an aerosol-enabled Multiscale Modeling Framework, Journal of Advances in Modeling Earth Systems, 6, 998-1015, 2014.

© Author(s) 2017. CC BY 4.0 License.

List of tables and figures

© Author(s) 2017. CC BY 4.0 License.

809 Figure 11: Vertical profiles for the mean observed ice water content from CALIPSO, and the simulated ice water
810 content from CTRL and DUST for dust events on March 21, April 1, April 9, and April 23, 2012.

811 Figure 12: Vertical profiles for the mean observed ice water content from CALIPSO, and the simulated ice water
812 content with various c_f for the dust events on March 21, April 1, April 9, and April 23, 2012.

813 Figure 13: Vertical profiles for the mean observational ice water content from CALIPSO, and the simulated ice water
814 content with threshold RH of 105% and 100% with respect to ice for the dust events on March 21, April 1, April 9,
815 and April 23, 2012.

816

Atmos. Chem. Phys. Discuss., https://doi.org/10.5194/acp-2017-754
Manuscript under review for journal Atmos. Chem. Phys.
Discussion started: 13 October 2017
© Author(s) 2017. CC BY 4.0 License.

Atmospheric Chemistry and Physics Discussions

Table 1: Performance statistics for the model in simulating surface PM_{10} concentrations at environmental monitoring stations during the simulation period.

STATION	LOCATION	MB	ME	RMSE	r
XCNAQ77	BAOTOU	-36.18	80.43	94.88	0.59
XCNAQ79		-10.05	75.83	106.58	0.62
XCNAQ346	SHIZUISHAN	72.46	121.18	317.73	0.79
XCNAQ347		17.64	147.95	294.71	0.75
XCNAQ340	JINCHANG	-108.73	109.09	128.56	0.77
XCNAQ342		-18.65	46.07	64.78	0.70
XCNAQ335	YAN'AN	-38.93	99.05	149.44	0.68
XCNAQ336		-60.15	124.74	166.89	0.60
XCNAQ344	YINCHUAN	33.97	112.26	240.27	0.87
CN_1487		-39.62	155.83	249.00	0.62
AVERAGE		-18.84	107.24	181.28	0.70

MB: mean bias; ME: mean error; RMSE: root mean squared error; r: correlation coefficient.

Atmos. Chem. Phys. Discuss., https://doi.org/10.5194/acp-2017-754
Manuscript under review for journal Atmos. Chem. Phys.
Discussion started: 13 October 2017
© Author(s) 2017. CC BY 4.0 License.

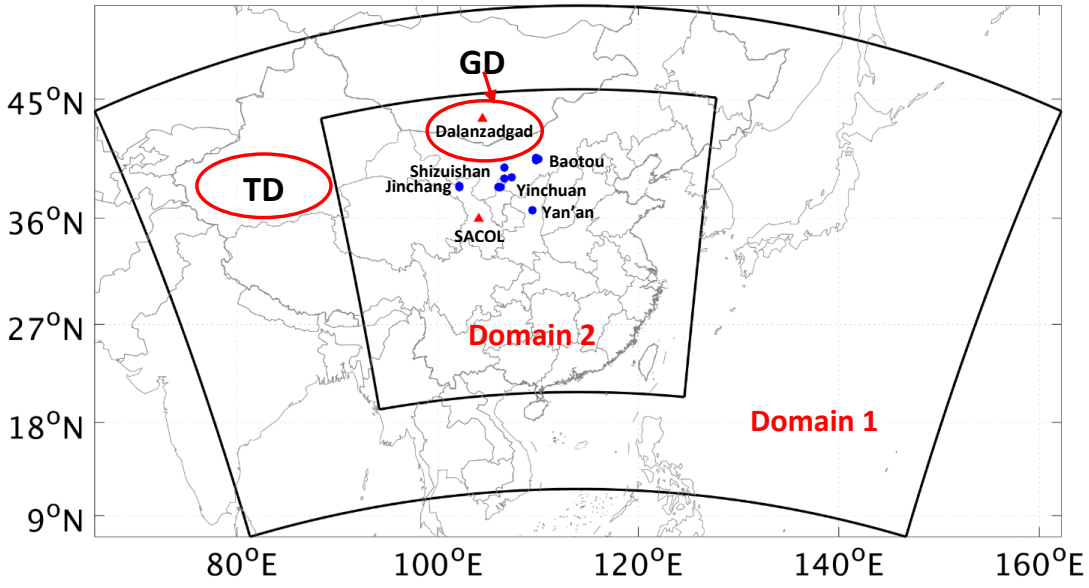

Figure 1: Nested domain set for the simulations. Blue dots represent the weather stations used for model validation. TD: the Taklimakan Desert; GD: The Gobi Desert.

Atmos. Chem. Phys. Discuss., https://doi.org/10.5194/acp-2017-754
Manuscript under review for journal Atmos. Chem. Phys.
Discussion started: 13 October 2017
© Author(s) 2017. CC BY 4.0 License.

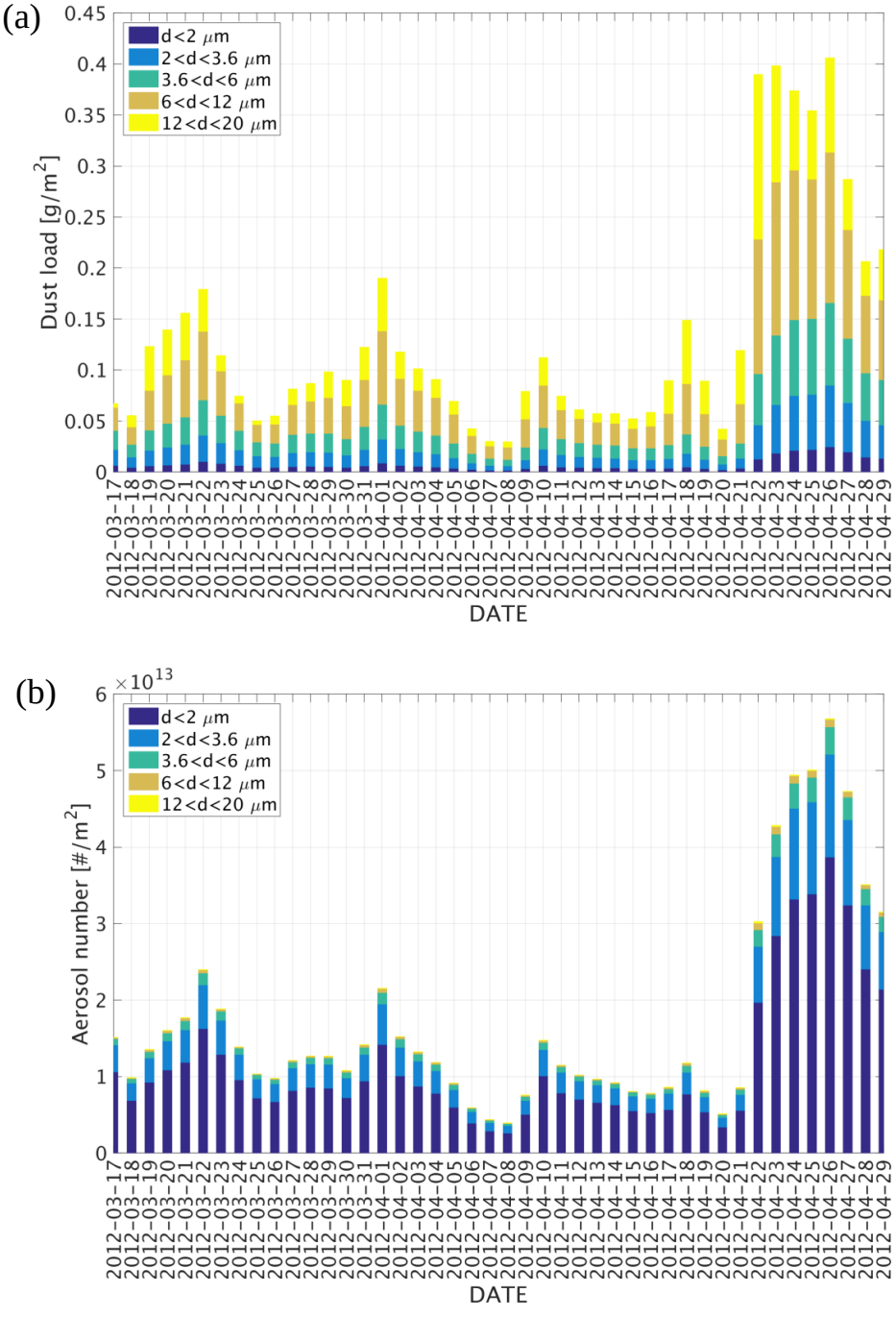

Figure 2: Time series of spatially averaged daily dust mass load (a) and daily number density of ice-friendly aerosol (b) over East Asia (domain 1) during the simulation period.

Atmos. Chem. Phys. Discuss., https://doi.org/10.5194/acp-2017-754
Manuscript under review for journal Atmos. Chem. Phys.
Discussion started: 13 October 2017
© Author(s) 2017. CC BY 4.0 License.

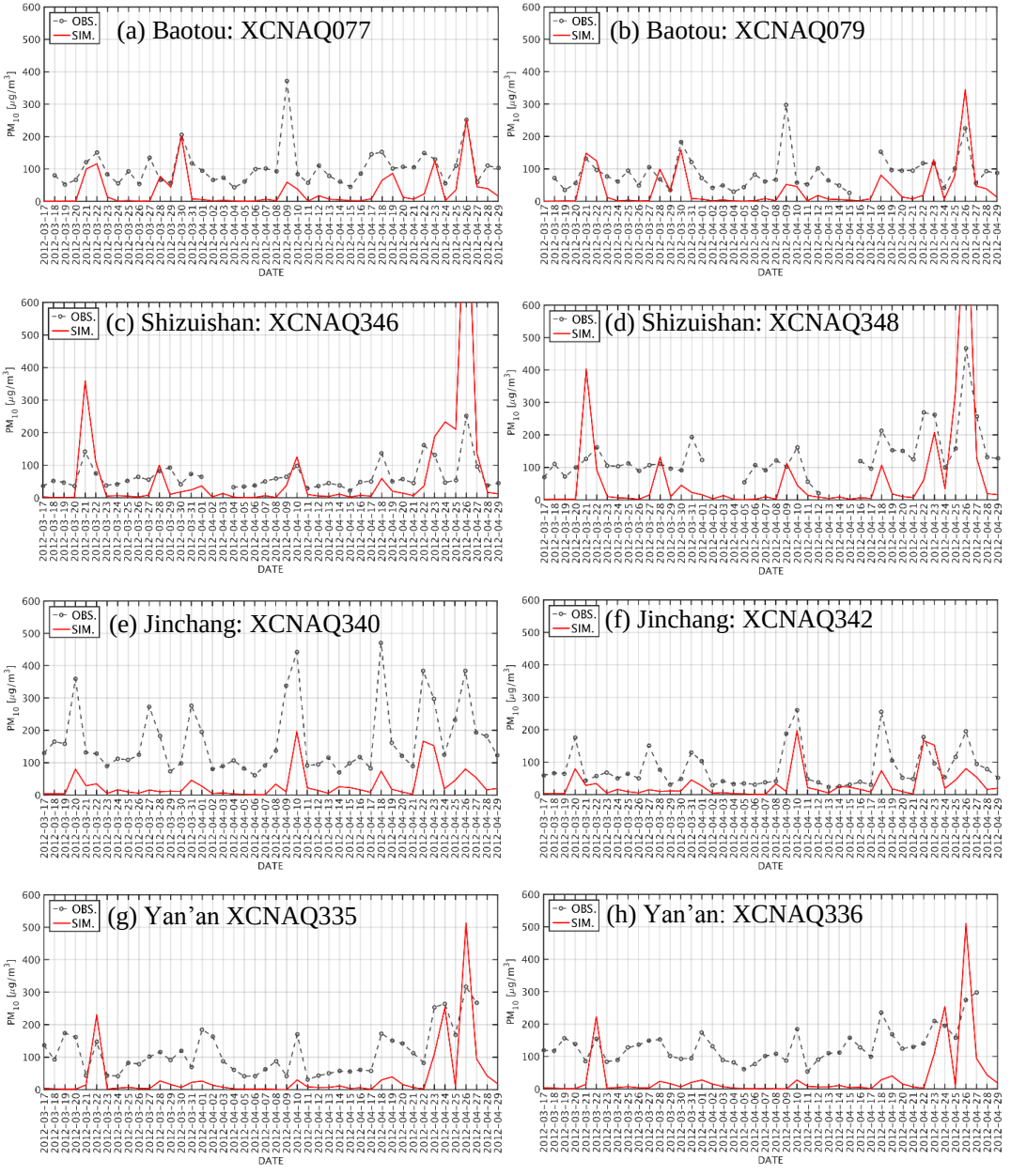

Figure 3: Time series of hourly observed and simulated surface PM_{10} concentrations at various environmental monitoring stations.

Atmos. Chem. Phys. Discuss., https://doi.org/10.5194/acp-2017-754
Manuscript under review for journal Atmos. Chem. Phys.
Discussion started: 13 October 2017
© Author(s) 2017. CC BY 4.0 License.

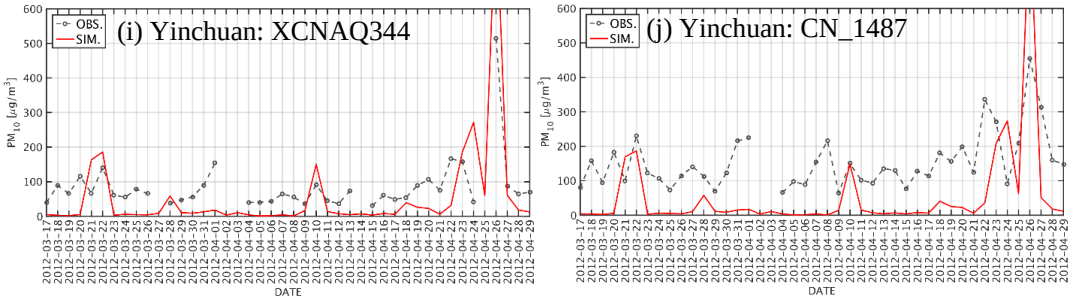

Figure 3: Continued.

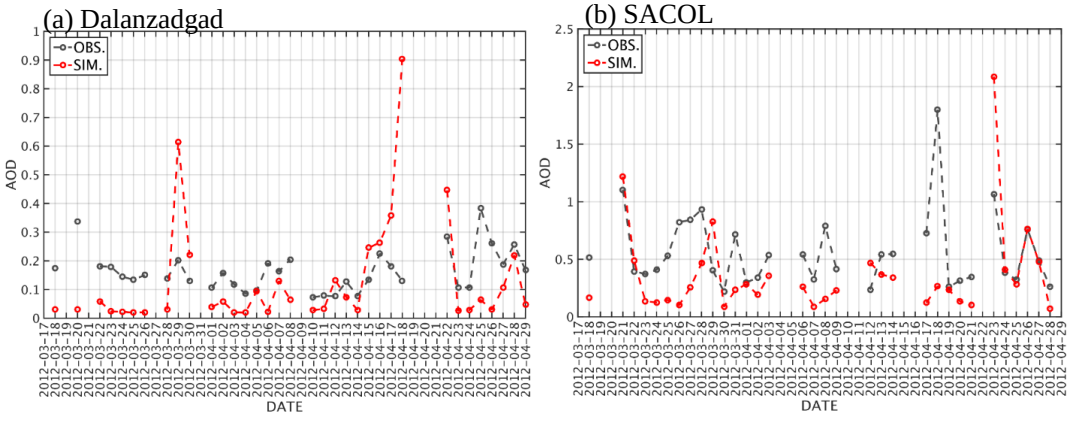

Figure 4: Time series of daily mean observed and simulated aerosol optical depths at Dalanzadgad (a) and SACOL (b).

Atmos. Chem. Phys. Discuss., https://doi.org/10.5194/acp-2017-754
Manuscript under review for journal Atmos. Chem. Phys.
Discussion started: 13 October 2017
© Author(s) 2017. CC BY 4.0 License.

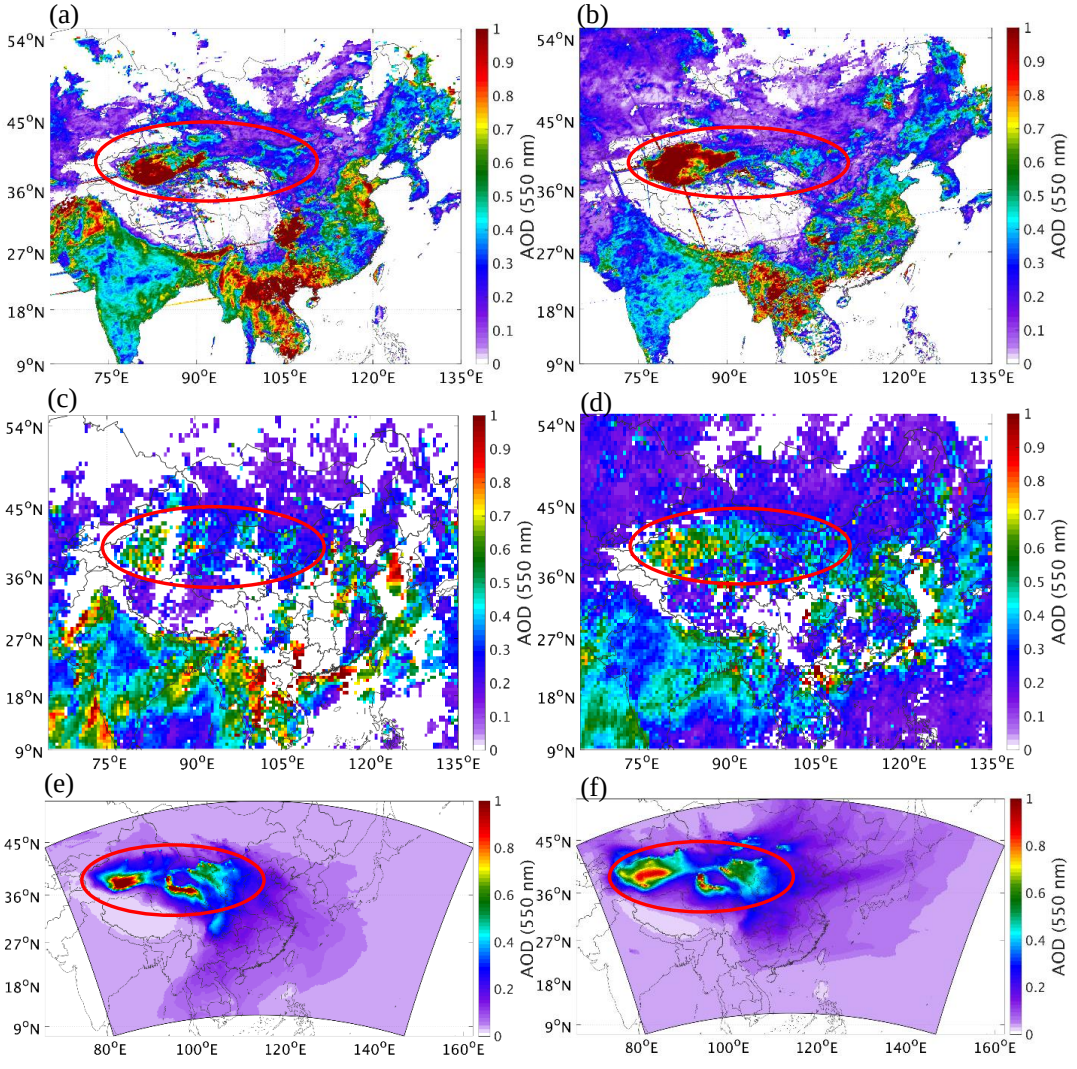

Figure 5: Spatial distributions of monthly mean AOD from MODIS observations (a, b), MISR observations (c, d), and simulation results (e, f) for March (left panel) and April (right panel) of 2012.

Atmos. Chem. Phys. Discuss., https://doi.org/10.5194/acp-2017-754
Manuscript under review for journal Atmos. Chem. Phys.
Discussion started: 13 October 2017
© Author(s) 2017. CC BY 4.0 License.

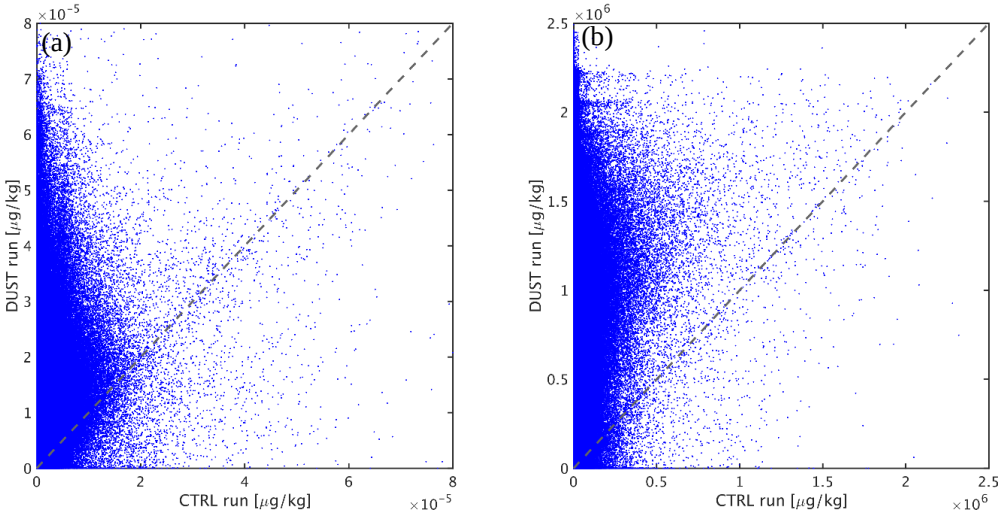

Figure 6: Simulated cloud ice mixing ratio (a) and cloud ice crystal number concentration (b) at each data point from CTRL and DUST.

Atmos. Chem. Phys. Discuss., https://doi.org/10.5194/acp-2017-754
Manuscript under review for journal Atmos. Chem. Phys.
Discussion started: 13 October 2017
© Author(s) 2017. CC BY 4.0 License.

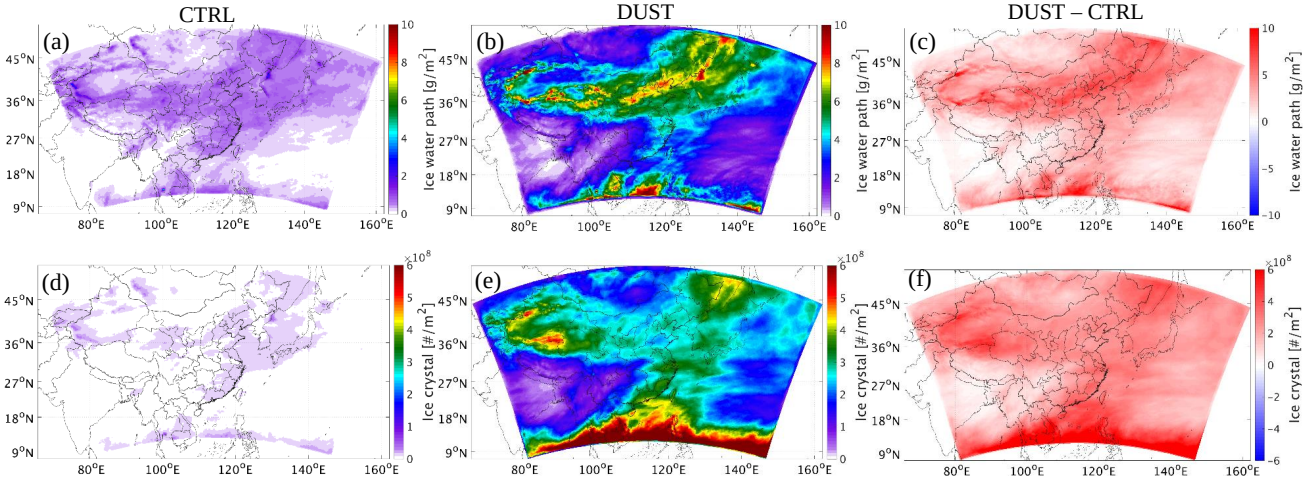

Figure 7: Spatial distributions for the temporal mean simulated cloud ice water path (a-c) and ice crystal number density (d-f) from CTRL (left panel), DUST (middle panel), and the difference between CTRL and DUST (right panel) over East Asia (domain 1) during the simulation period.

Atmos. Chem. Phys. Discuss., https://doi.org/10.5194/acp-2017-754
Manuscript under review for journal Atmos. Chem. Phys.
Discussion started: 13 October 2017
© Author(s) 2017. CC BY 4.0 License.

Atmospheric Chemistry and Physics Discussions

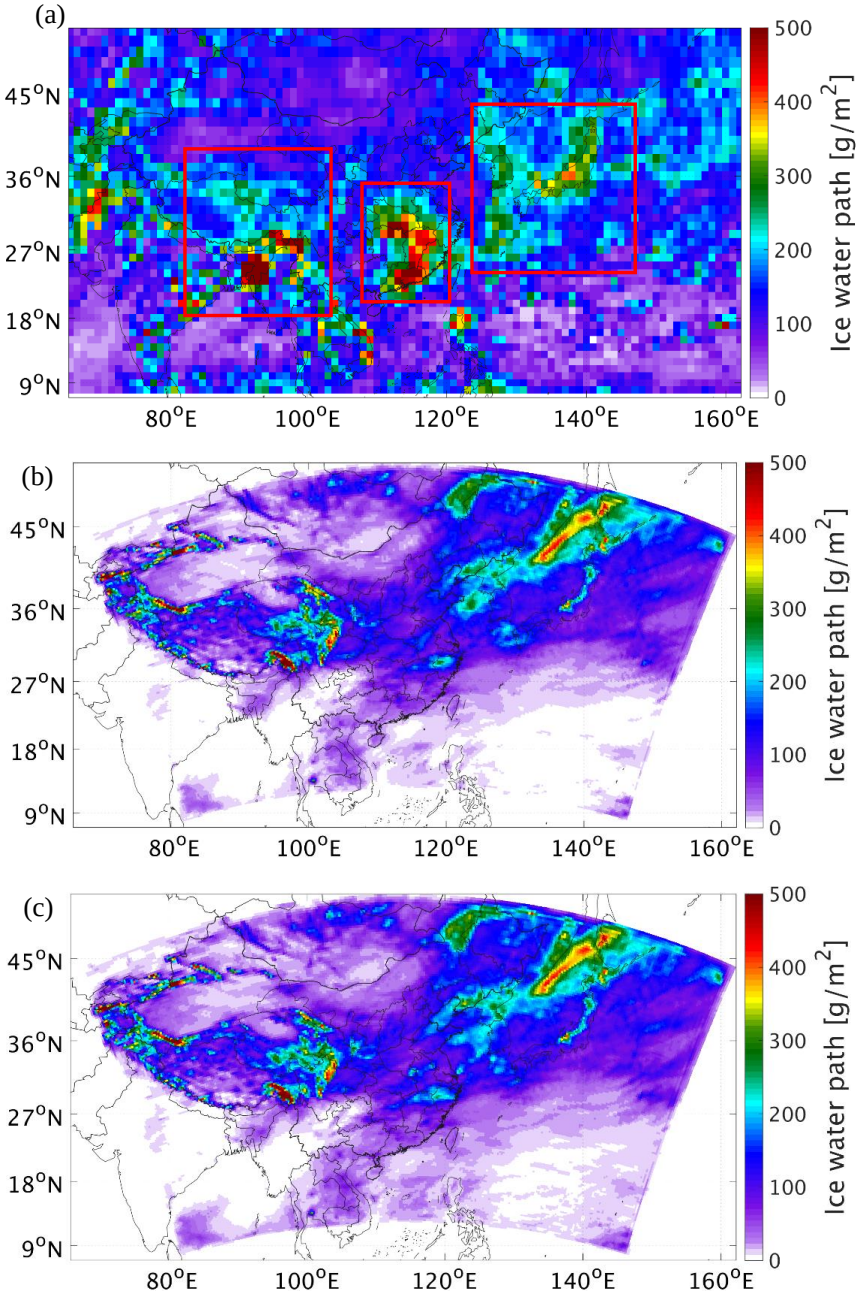

Figure 8: Spatial distribution for the mean ice water path (a) from MODIS observations, and the simulation results of CTRL (b) and DUST (c) during the simulation period.

Atmos. Chem. Phys. Discuss., https://doi.org/10.5194/acp-2017-754
Manuscript under review for journal Atmos. Chem. Phys.
Discussion started: 13 October 2017
© Author(s) 2017. CC BY 4.0 License.

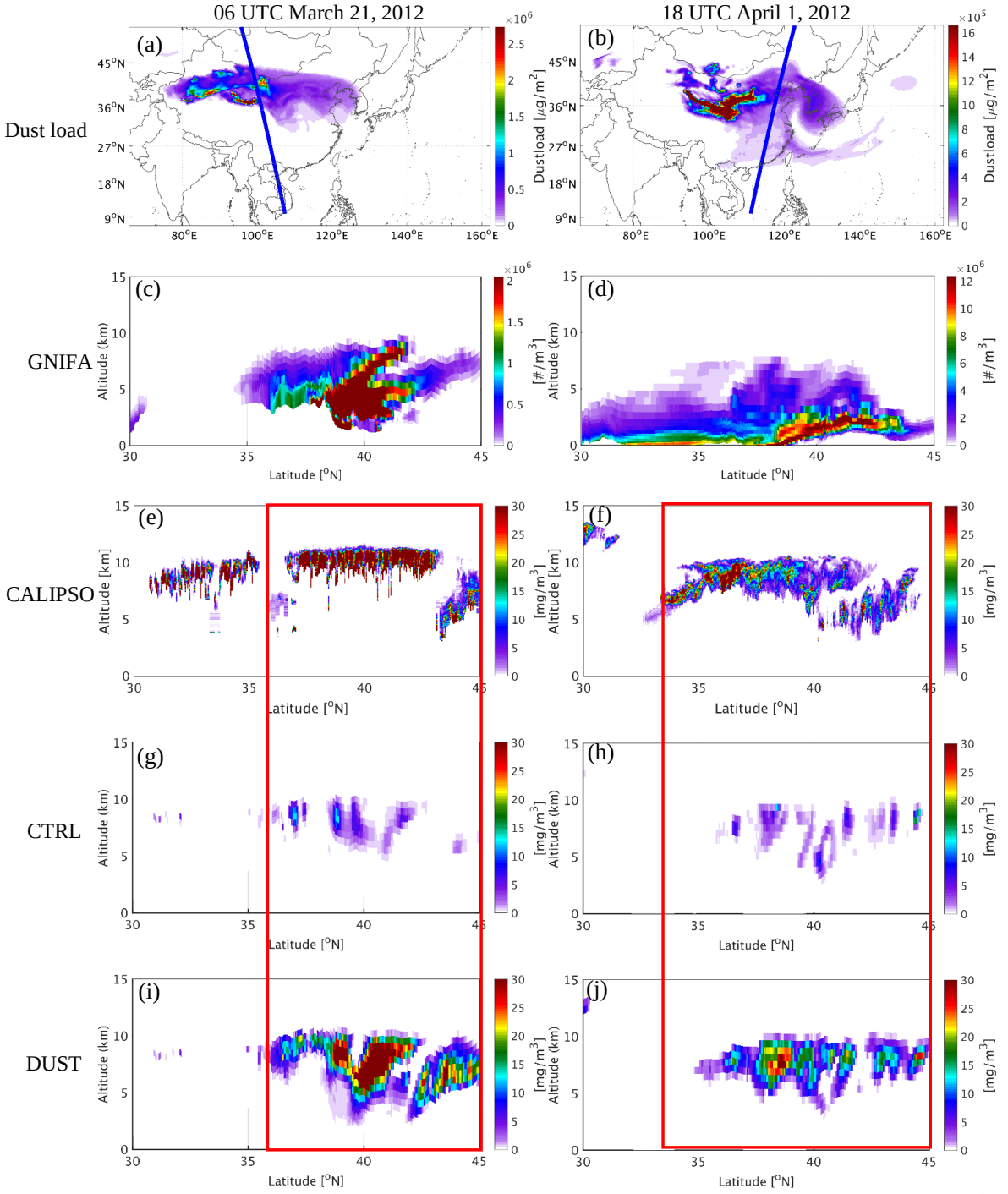

Figure 9: Spatial distribution for simulated dust load and satellite scanning track (a, b), the simulated vertical profile of ice-friendly aerosol (GNIFA) number concentration (c, d), the CALIPSO vertical profile of ice water content (e, f), and the simulated vertical profile of ice water content from CTRL (g, h) and DUST (i, j) for the case on March 21 (left panel) and April 1 (right panel) of 2012.

Atmos. Chem. Phys. Discuss., https://doi.org/10.5194/acp-2017-754
Manuscript under review for journal Atmos. Chem. Phys.
Discussion started: 13 October 2017
© Author(s) 2017. CC BY 4.0 License.

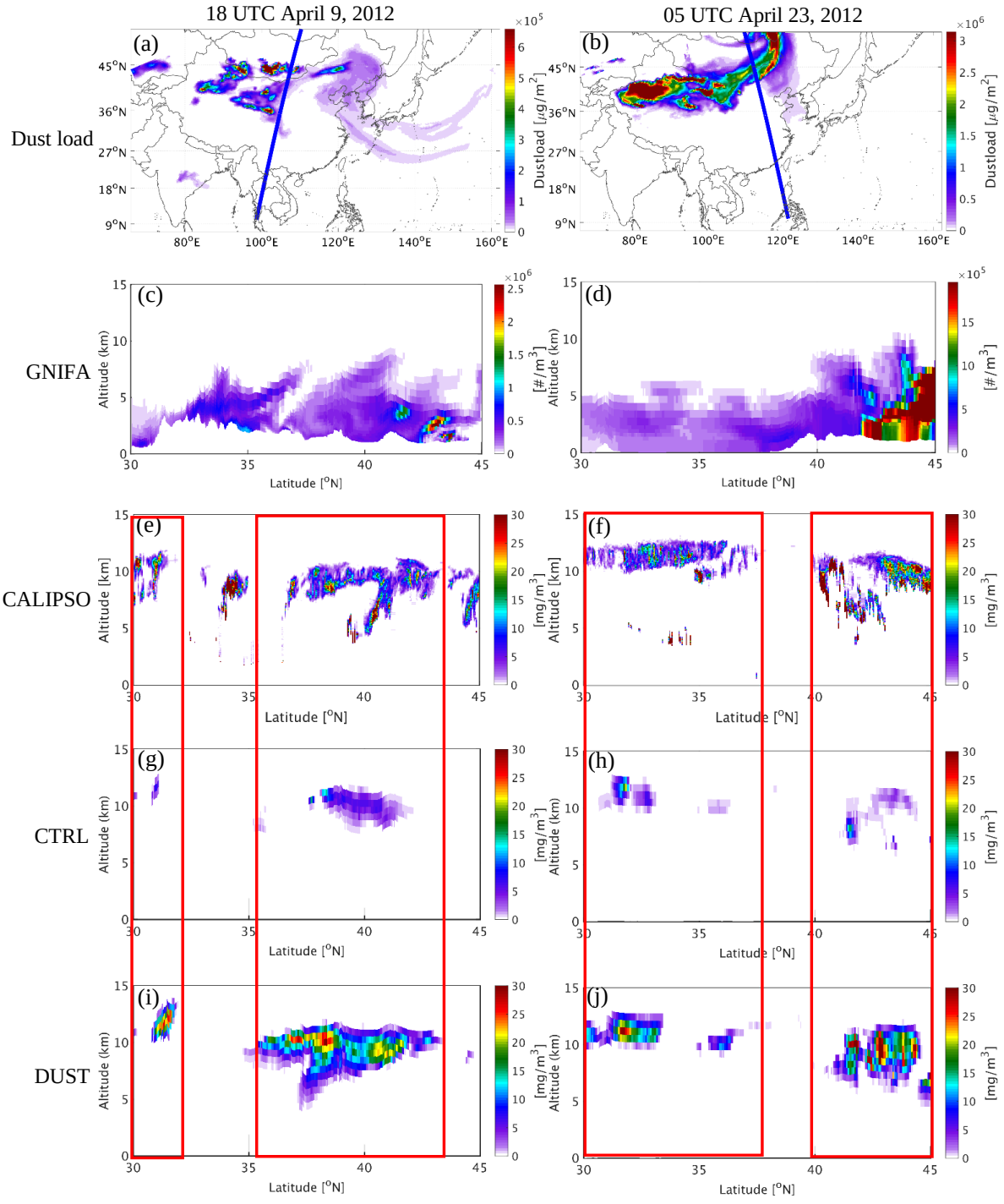

Figure 10: As Figure 9 but for the cases on April 9 (left panel) and April 23, (right panel) of 2012.

Atmos. Chem. Phys. Discuss., https://doi.org/10.5194/acp-2017-754
Manuscript under review for journal Atmos. Chem. Phys.
Discussion started: 13 October 2017
© Author(s) 2017. CC BY 4.0 License.

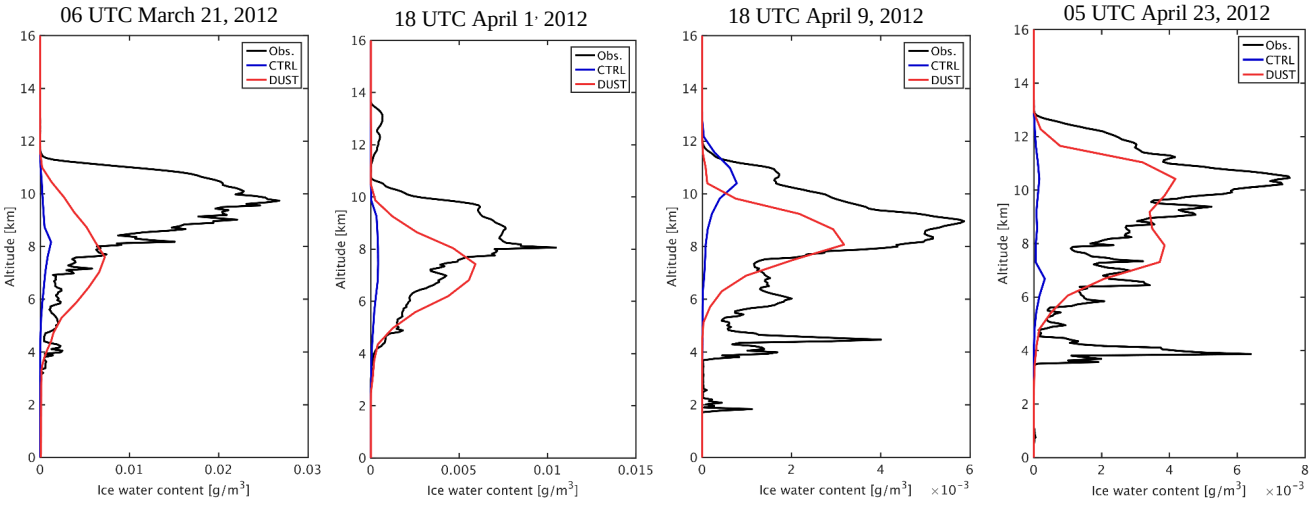

Figure 11: Vertical profiles for the mean observed ice water content from CALIPSO, and the simulated ice water content from CTRL and DUST for dust events on March 21, April 1, April 9, and April 23, 2012.

Atmos. Chem. Phys. Discuss., https://doi.org/10.5194/acp-2017-754
Manuscript under review for journal Atmos. Chem. Phys.
Discussion started: 13 October 2017
© Author(s) 2017. CC BY 4.0 License.

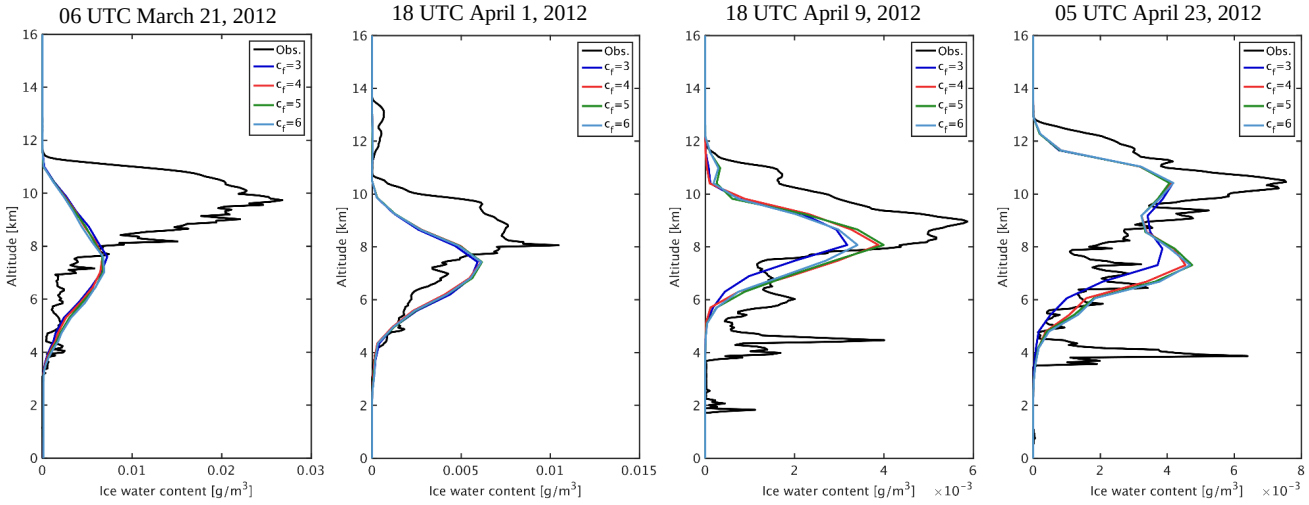

Figure 12: Vertical profiles for the mean observed ice water content from CALIPSO, and the simulated ice water content with various c_f for the dust events on March 21, April 1, April 9, and April 23, 2012.

Atmos. Chem. Phys. Discuss., https://doi.org/10.5194/acp-2017-754
Manuscript under review for journal Atmos. Chem. Phys.
Discussion started: 13 October 2017
© Author(s) 2017. CC BY 4.0 License.

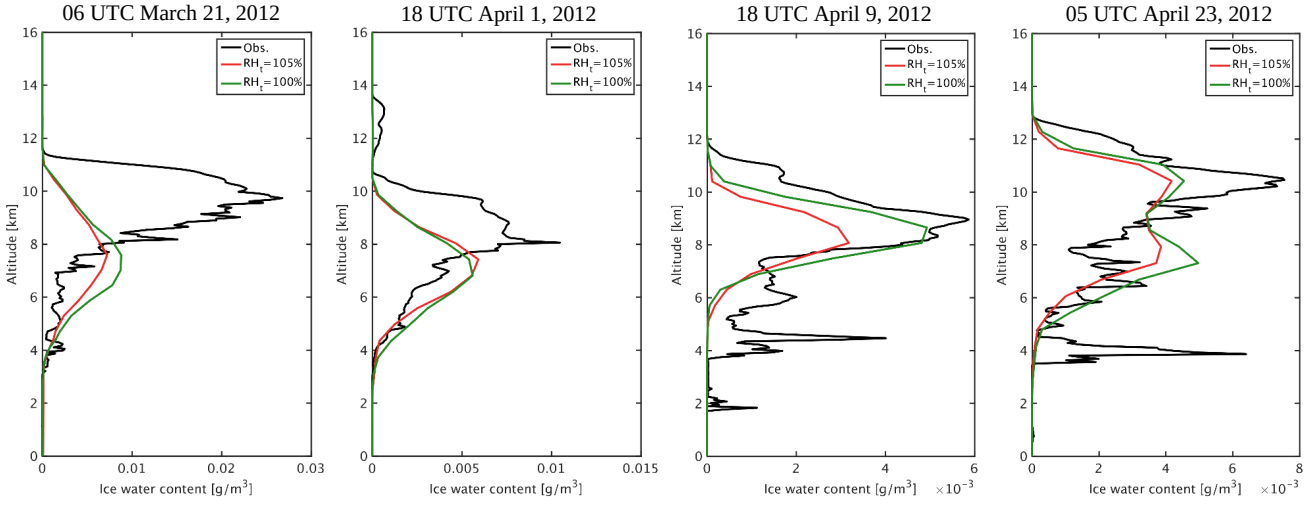

Figure 13: Vertical profiles for the mean observational ice water content from CALIPSO, and the simulated ice water content with threshold RH of 105% and 100% with respect to ice for the dust events on March 21, April 1, April 9, and April 23, 2012.